NOVA SCHOOL OF SCIENCE & TECHNOLOGY

DEPARTMENT OF
LIFE SCIENCES, MATERIALS SCIENCE,
PHYSICS AND CHEMISTRY

CAROLINA RAMOS PINTA

BSc in Human Biology

TISSUE ENGINEERING OF CARDIAC ARRHYTHMIC MODELS FOR DRUG DEVELOPMENT

MASTER IN Biomaterials and Nanomedicine

NOVA University Lisbon

September, 2024

DEPARTMENT OF
LIFE SCIENCES, MATERIALS SCIENCE,
PHYSICS AND CHEMISTRY

TISSUE ENGINEERING OF CARDIAC ARRHYTHMIC MODELS FOR DRUG DEVELOPMENT

CAROLINA RAMOS PINTA

BSc in Human Biology

Adviser: Henrique Vazão de Almeida
Researcher, CENIMAT|i3N *NOVA University Lisbon*

Co-adviser: José Inácio
Researcher, NMS *NOVA University Lisbon*

MASTER IN BIOMATERIALS AND NANOMEDICINE

NOVA University Lisbon
September, 2024

Tissue Engineering of Cardiac Arrhythmic Models For Drug Development

Aos meus pais e irmã.

ACKNOWLEDGMENTS

O desenvolvimento deste projeto não teria sido possível sem o apoio e orientação dos Professores Henrique Almeida e José Inácio. Agradeço pela oportunidade que me deram de integrar esta experiência inovadora com a vossa total disponibilidade e auxílio na superação de todos os obstáculos ao longo deste ano. À Professora Marta Corvo, um grande obrigada pela ajuda e paciência em todos os passos de sintetização de GelMA. Ao Professor Ricardo Andrade, obrigada pelas explicações incansáveis sobre o tema: Reologia. Ao Dr. Santanu Jana por disponibilizar a solução de MXenes utilizada no projeto. Por fim, mas não menos importante, agradeço a todos os integrantes do CENIMAT|i3N pela amabilidade com que me acolheram neste desafio e por terem estado sempre predispostos a ajudar-me em tudo o que necessitei, sem qualquer hesitação.

A minha família foi o meu maior suporte. Obrigada por ouvirem pacientemente todos as minhas frustrações e por me relembrarem que os dias maus também fazem parte do sucesso. Não esquecerei de todas as palavras de carinho que proferiram quando os dias em laboratório eram longos, foram a minha maior motivação e isto não tem preço!

Quero ainda agradecer às minhas colegas de Mestrado Eduarda, Lara e Lydia que me acompanharam desde o primeiro dia, por terem tornado todos os trabalhos de grupo mais leves, por me terem ajudado a carregar este curso e por terem definido tão bem o conceito de trabalho de equipa.

À minha colega de bancada, Teresa, um grande obrigada pela amiga que se tornou nas longas jornadas de laboratório, pelos conhecimentos que me transmitiu, pelos almoços tranquilizantes, pelos desabafos, pelas gargalhadas e, claro, pela ajuda na compreensão de alguns dos comandos do Excel.

"I put my heart and soul into my work and I have lost my mind in the process" (Van Gogh)

.

ABSTRACT

Cardiovascular diseases, particularly arrhythmias, remain a major global health challenge, characterized by high mortality rates and significant morbidity. The increasing prevalence of these conditions has spurred interest in innovative approaches to cardiac tissue engineering, aiming to develop functional tissues that can mimic the properties of native cardiac structures. This dissertation focuses on the development of bioinks designed to replicate the extracellular matrix (ECM) characteristics of cardiac tissue, specifically targeting conductivity and biocompatibility to enhance cardiomyocyte maturation.

The primary objective of this research was to create Gelatin Methacryloyl (GelMA) hydrogels incorporated with conductive nanoparticles, facilitating the bioprinting of cardiac tissue models. These models are intended to emulate the electrical conductivity and anisotropic architecture of heart tissue, which are crucial for proper cardiac function. The study emphasizes the importance of these properties in promoting the growth and differentiation of cardiomyocytes, which are essential for effective tissue regeneration.

Despite the challenges encountered, including the inability to successfully develop an in vitro model of arrhythmia, the findings contribute valuable insights into the potential of bioink formulations and bioprinting techniques in cardiac tissue engineering.

In conclusion, while the goal of creating a functional in vitro arrhythmia model was not achieved, this dissertation lays the groundwork for future studies aimed at advancing cardiac tissue engineering. The proposed methodologies and materials offer promising avenues for developing cardiac models that could ultimately aid in drug development and therapeutic strategies for treating arrhythmias and other cardiovascular diseases.

Keywords: Arrhythmia, Regeneration, GelMA, MXenes, 3D Bioprinting, Cardiomyocytes

RESUMO

As doenças cardiovasculares, particularmente as arritmias, continuam a ser um grande desafio para a saúde a nível mundial, caracterizado por elevadas taxas de mortalidade e morbilidade significativa. O aumento da prevalência destas condições tem estimulado o interesse em abordagens inovadoras à engenharia de tecidos cardíacos, com o objetivo de desenvolver tecidos funcionais que possam imitar as propriedades das estruturas cardíacas nativas. Esta dissertação centra-se no desenvolvimento de biotintas concebidas para replicar as caraterísticas da matriz extracelular (MEC) do tecido cardíaco, visando especificamente a condutividade e a biocompatibilidade para melhorar a maturação dos cardomiócitos.

O principal objetivo desta investigação foi criar hidrogéis de Gelatina Metacriloil (GelMA) incorporados com nanopartículas condutoras, facilitando a bioimpressão de modelos de tecido cardíaco. Estes modelos destinam-se a emular a condutividade eléctrica e a arquitetura anisotrópica do tecido cardíaco, que são cruciais para a função cardíaca adequada. O estudo sublinha a importância destas propriedades na promoção do crescimento e diferenciação dos cardomiócitos, que são essenciais para uma regeneração eficaz dos tecidos.

Apesar dos desafios encontrados, incluindo a incapacidade de desenvolver com sucesso um modelo in vitro de arritmia, os resultados contribuem com informações valiosas sobre o potencial das formulações de biotintas e das técnicas de bioimpressão na engenharia de tecidos cardíacos.

Em conclusão, embora o objetivo de criar um modelo funcional de arritmia in vitro não tenha sido alcançado, esta dissertação estabelece as bases para estudos futuros destinados a fazer avançar a engenharia de tecidos cardíacos. As metodologias e materiais propostos oferecem vias promissoras para o desenvolvimento de modelos cardíacos que poderão, em última análise, ajudar no desenvolvimento de medicamentos e estratégias terapêuticas para o tratamento de arritmias e outras doenças cardiovasculares.

Palavras chave: Arritmia, Regeneração, GelMA, MXenes, Bioimpressão 3D, Cardomiócitos

CONTENTS

LIST OF FIGURES

List of Tables

ACRONYMS

2D	Two Dimensional
3D	Three Dimensional
AFM	Atomic Force Microscopy
CVDs	Cardiovascular Diseases
DM	Degree of Methacrylation
EBB	Extrusion-Based Bioprinting
ECM	Extracellular Matrix
FRESH	Reversible Incorporation of Suspended Hydrogels
GelMA	Gelatin Methacryloyl
hiPSC	Human induced pluripotent Stem Cell
hiPSC-CMs	hiPSC-derived Cardiomyocytes
LAP	Lithium phenyl-2,4,6-trimethylbenzoylphosphinate
MAA	Methacrylic Anhydride
MMP	Matrix Metalloproteinase
MX	MXenes
NMR	Nuclear Magnetic Resonance
PBS	Phosphate Buffer Saline

PDA-rGO	Polydopamine-Reduced Graphene Oxide
PEG	Polyethylene Glycol
PSVT	Paroxysmal Supraventricular Tachycardia
RGD	Arginine-Glycine-Aspartic Acid
SEM	Scanning Electron Microscopy
SLAM	Suspended Layer Additive Manufacturing
SWIFT	Sacrificial Writing on Functional Tissue
UV	Ultraviolet

SYMBOLS

G'	Storage Modulus
G''	Loss Modulus
MPa	MegaPascal
Pa	Pascal
kPa	KiloPascal
mm	Millimeter
E	Young's Modulus
µL	Microliter
ml	Milliliter
(w/v)	Weight per volume
≤	Less than or Equal to

1

INTRODUCTION

1.1 Cardiovascular Diseases

Cardiovascular diseases (CVDs) are the leading cause of death globally, responsible for an estimated 17.9 million deaths each year. Among these, arrhythmias are a significant subset, contributing to the high rates of morbidity and mortality worldwide [1-4]. It manifests in various forms, including ischemic disease, arrhythmias, and congenital diseases, which can progress to heart failure. Robust disease models are essential to better comprehend the mechanics behind cardiac disease [3][2].

Modern pharmaceutical technology has advanced significantly, leading to significant advancements in CVD medical care. Nevertheless, there are still certain obstacles that need to be solved. In addition to having numerous side effects and poor efficacy, most small chemical compounds used to treat CVD also have low patient compliance. Natural products are becoming increasingly important for novel medications since they are biocompatible, pharmacologically active, and have low toxicity [2].

1.1.1 Arrhythmia

An arrhythmia is a heartbeat issue where the heartbeat is too fast, too slow, or with an irregular rhythm. These irregular heartbeats can indicate insufficient blood flow to the body and disrupt the heart's normal functioning, leading to complications like palpitations, fainting, and stroke [5][6].

Arrhythmias are classified into tachyarrhythmia (fast heart rates) and bradyarrhythmia (slow heart rates). Arrhythmias are irregular heartbeats in the atria (upper chambers) or ventricles (lower chambers). They can cause slow, fast, or irregular heartbeats depending on the

affected part of the heart. Bradycardia is a resting heart rate slower than 60 beats per minute, which may be normal for some people, especially young or physically fit individuals. Tachycardia is a resting heart rate faster than 100 beats per minute and may also have an irregular heartbeat [6].

The opening to the lower chambers, known as the atria, is where supraventricular arrhythmias begin. The most prevalent kind, atrial fibrillation, causes the heart to pulse faster than 400 beats per minute. The heart's upper chambers may pulse 250–350 times per minute because of atrial flutter. An issue with electrical signals that start in the upper chambers and move to the lower chambers is the cause of paroxysmal supraventricular tachycardia (PSVT), which results in additional heartbeats. The heart's lower chambers, known as the ventricles, are where ventricular arrhythmias begin. These arrhythmias are typically serious and necessitate emergency medical attention. Ventricular tachycardia is characterized by rapid, regular heartbeats that might extend for several seconds or more. Ventricular tachycardia lasting a few beats is usually not problematic, but if it persists for longer than a few seconds, it may result in more severe arrhythmias, like ventricular fibrillation [5-7].

Procedures or medication can be used to treat them. Arrhythmias, however, have the potential to cause serious illnesses including stroke, heart failure, or cardiac arrest if they are not addressed. They can also harm the brain, heart, or other organs. Drug therapies, invasive surgeries, or the use of electronic devices like pacemakers and defibrillators are frequently used in management. However, these methods have several drawbacks, including being invasive, having poor efficacy, and causing severe side effects. Consequently, novel approaches are required to successfully treat and manage arrhythmias [7-11].

1.2 Regenerative Medicine

Regenerative medicine is an interdisciplinary area that uses synthetic biological alternatives or the body's natural healing processes to replace or repair damaged tissues and organs. It covers a wide range of techniques, such as tissue engineering, gene therapy, and stem cell therapy. Regenerative medicine aims to repair damaged tissues and organs to their original state, providing treatment for illnesses that are now incurable or exceedingly difficult to treat. This area of study makes use of developments in stem cell biology, biomaterials, and bioengineering to create treatments that can, among other things, heal degenerative illnesses, regenerate heart tissue, and repair spinal cord injuries [12][13].

1.3 Tissue Engineering

Tissue engineering, a critical component of regenerative medicine, combines principles of biology, engineering, and materials science to develop biological substitutes that can restore, maintain, or improve tissue function [14]. Scaffolds are essential to tissue engineering because they offer a three-dimensional framework for cell adhesion, proliferation, and differentiation [15].

1.4 Hydrogels

Hydrogels are three-dimensional hydrophilic polymer networks that can swell in water and grow larger than their initial weight without dissolution. They have tunable physical and chemical properties that comonomers, crosslink density, and synthetic conditions can alter. Hydrogels are crucial in biomedical fields like tissue engineering, regenerative medicine, and drug delivery. Like the natural extracellular matrix, they provide mimetic conditions for in vitro cell culture. Hydrogels are divided into natural and synthetic types, with natural hydrogels having better biocompatibility, contributing to cellular viability, multiplication, differentiation, and locomotion [16].

Hydrogels, including collagen, gelatin, Matrigel, alginate, fibrin, poly (2-hydroxyethyl methacrylate) (PHEMA), poly (N-isopropyl acrylamide), and poly(ethylene glycol) (PEG), are commonly used in cardiac tissue engineering. These substances can be used alone or in combination with cells and can contain growth agents for tissue development [17]. With advancements in material science, hydrogel-based scaffolds have significant potential in tissue engineering [16].

Biopolymers can be used to design biomaterials that mimic the extracellular matrix (ECM), providing a promising method for 3D tissue engineering and regenerative technologies in medicine. The ECM of native mammalian tissues is a collagen-based hydrogel with a complex supramolecular structure [18].

The ideal scaffold for cardiac tissue engineering should combine mechanical and biological properties to facilitate cardiomyocyte attachment, growth, alignment, elongation, and flexibility for sustained expansion and contraction cycles, promoting cellular alignment and elongation [19].

1.5 Gelatin Methacryloyl

Gelatin, a naturally occurring hydrophilic polymer, is obtained from native collagen through denaturation and partial hydrolysis and has many benefits, including biocompatibility, solubility, degradability, and ease of acquisition. Compared to collagen, it is less antigenic. It preserves the peptide sequence arginine-glycine-aspartic acid (RGD), which is crucial for the interaction of cells with the surrounding ECM, stimulating cell adhesion, proliferation, and differentiation. Its thermostability is low. Nevertheless, chemical crosslinking may make it less biocompatible because of potentially toxic crosslinking agents [20][21].

Van Den Bulcke et al. initially presented Gelatin Methacryloyl (GelMA) in 2000. It is a modified form of gelatin created through a reaction with methacrylic anhydride (MAA), as shown in Figure 1.1. Methacrylation can be achieved by forming a chemically more stable amide group, while physically gelled gelatin may reduce stability. Because methacryloyl groups are present, the modified gelatin exhibits photocrosslinking and a temperature-dependent solid-liquid transition. A water solution of modified gelatin crosslinks under ultraviolet (UV) light upon adding a photoinitiator, producing GelMA hydrogels with superior thermostability

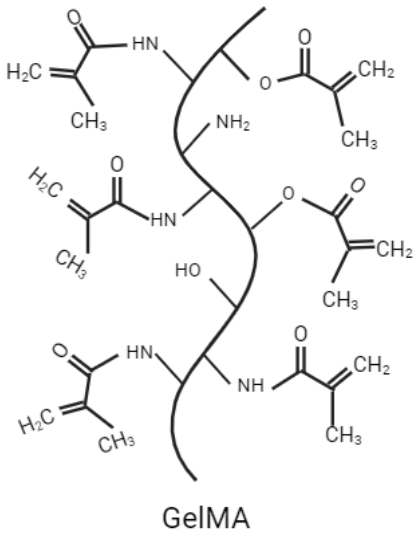

Figure 1.1 — Gelatin Methacryloyl. Adapted from [116].

and tunable mechanical properties. These hydrogels preserve the arginine-glycine-aspartic acid (RGD) and matrix metalloproteinase (MMP) sequences and their biocompatibility and degradation characteristics. They are also very adaptable to the demands of different applications [20-22].

GelMA's biocompatibility makes it suitable for various biomedical applications, including tissue engineering and regenerative medicine. Its ability to support cell adhesion and proliferation and its modifiable stiffness and degradation rates make GelMA an ideal candidate for creating scaffolds for cardiac tissue engineering [23].

1.6 Conductive Materials

Native cardiac tissue possesses the necessary electrophysiological characteristics for successful operation. To imitate these qualities, materials must be electroconductive. As a result, conductive scaffolds can be made by mixing nanocomposites with the hydrogel. MXenes will be the nanocomposites in this study that provide electrical characteristics [24].

1.6.1 MXenes

Integrating conductive materials into the scaffolds is crucial for successful cardiac tissue engineering to promote the synchronized contraction of cardiomyocytes, helping to regenerate the unhealthy tissues. MXenes are a class of two-dimensional transition metal carbides, nitrides, and carbonitrides that have gained attention as prospective conductive materials because of their remarkable mechanical attributes, biocompatibility, and electrical conductivity [25][26].

MXenes can be added to hydrogels to form conductive scaffolds or functionalized to improve their compatibility with biological tissues. Adding MXenes to GelMA hydrogels may produce a composite material that imitates the naturally conductive characteristics of cardiac tissue, offering structural support and making electrical signal propagation easier. This composite material, combined with a polymer and cells, may close the gap between unhealthy and healthy tissues, encouraging the myocardium's ability to regenerate and function [26].

Two-dimensional (2D) materials called MXenes are employed in a variety of industries. Tissue engineering is among them because of its special mechanical, electrical, and biological characteristics, chemical stability, wide surface area, and hydrophilicity [27].

It has many functional groups, including -O, -F, and -OH, on the surface and is dispersible in aqueous solvents without aggregating [24][25] [28-31]. MXenes, whose general chemical formula is $Mn+1Xn$, where M is an early transition metal, n is an integer between 1 and 6, and X is carbon or nitrogen, are composed of transition metal nitrides, carbides, and carbonitrides [28][32].

These materials are conductive because of the free electrons connected to the transition metal nitrides, carbides, and carbonitrides. Additionally, MXenes are composed of elements commonly found in biological systems, including carbon (C), nitrogen (N), hydrogen (H), and oxygen (O) [25][27].

This substance has already been used in cardiac tissue engineering, with results demonstrating the alignment of cardiomyocytes derived from human induced pluripotent stem cells, a notable increase in the gap junction protein CX43 expressed in cardiomyocytes, no cytotoxicity, and an improvement in conduction velocity and synchronous beating [33].

1.7 Photoinitiators in GelMA Hydrogels

Compounds known as photoinitiators can absorb light and start the polymerization process, which is necessary for GelMA hydrogel production. The photoinitiator selection is crucial for the hydrogel's mechanical characteristics, biocompatibility, and cross-linking efficiency. Irgacure 2959 and lithium phenyl-2,4,6-trimethylbenzoylphosphinate (LAP), which are activated by UV and visible light, respectively, are commonly used photoinitiators. These photoinitiators allow hydrogels to develop in moderate environments while maintaining the viability and functionality of cells [34][35].

GelMA hydrogels can be effectively crosslinked by photoinitiators such as LAP (Figure 1.2), which preserve excellent cell viability while supplying the required structural integrity. This characteristic is especially crucial for cardiac tissue engineering applications, where it is necessary to compromise the scaffold's mechanical stability and the need to support living cells [36].

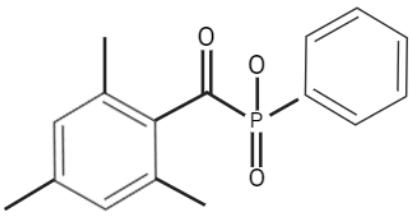

Figure 1.2 — LAP (lithium phenyl-2,4,6-trimethylbenzoylphosphinate)

LAP has been shown to have superior benefits over Irgacure 2959, including higher water solubility, a faster gelation rate, improved light absorption beyond 400 nm, and insurance cell viability [37]. It also has 50 times higher molar absorptivity, suggesting higher crosslinking efficiency. Garciá-Lizarribar et al. found that low concentration (0.1%) LAP is more promising than higher concentration (0.4%) Irgacure 2959 [38][39]. The photoinitiator absorbs UV light during

the photopolymer crosslinking process, generating free radicals that polymerize the photopolymer to produce the polymer network [37].

1.8 Cardiomyocytes

Since its introduction by Shinya Yamanaka's lab in 2007, human induced pluripotent stem cell (hiPSC) technology has been a valuable model for studies on human disorders. Stem cells have revolutionized regenerative medicine because they can differentiate into various types of cells and repair damaged tissues. Human induced pluripotent stem cells (hiPSCs) are particularly promising as they can be derived from adult cells, providing an ethically acceptable and unlimited source [40][41]. Human induced pluripotent stem cell-derived cardiomyocytes, or hiPSC-CMs, are characterized by their same genetic composition, expression of several heart-specific genes, and essential characteristics of human cardiomyocytes [40][45].

The heart contains several types of cells, including cardiomyocytes and endothelial cells, which are fundamental in health and disease. Cardiomyocytes, the main cellular component of the myocardium, are connected by gap junctions, adherents junctions, and desmosomes, facilitating coordinated contractions [42]. These cells are crucial for generating the force needed to pump blood. However, pathological conditions such as hypertension or myocardial infarction can cause hypertrophy, apoptosis, and necrosis in cardiomyocytes, further impairing cardiac function. The loss of these cells, such as in myocardial infarction and heart failure, impairs cardiac function and can lead to arrhythmias. Regeneration of functional cardiomyocytes is a fundamental goal in cardiac tissue engineering [41][45].

Cardiomyocyte regeneration is limited, with an annual renewal rate of around 1%, decreasing with age. This low regeneration rate is a significant challenge in the recovery of heart injury [43][45]. The unique structure and function of cardiomyocytes, including their role in excitation-contraction coupling, make them essential but difficult to replace when damaged. hiPSC-derived cardiomyocytes (hiPSC-CMs) offer significant potential in developing personalized therapies. These cells can be derived from the patient's cells, reducing the risk of immune rejection. In addition, hiPSC-CMs can model patient-specific arrhythmias in vitro, aiding in the study of disease mechanisms and developing targeted treatments [44].

1.9 In Vitro Models

1.9.1 2D and 3D Models

In vitro, 2D cell culture methods are used to study biological functions, but their simplicity makes complex structures challenging to simulate. Recent research suggests that 3D tissue models are superior for mimicking complex tissue or organ architecture due to their resolution and accuracy [46]. Models involving extracellular matrix proteins in human tissue are increasingly crucial for advanced application-based research, including drug testing and translational purposes. The extracellular matrix regulates cellular functions through biophysical and biochemical signals. 3D models using cells and proteins recreate native organs, aiding in understanding functions and generating personalized drug testing platforms [46]. Organ-on-the-chip technology simulates organ-level physiology, enabling bioengineering and designing complex biomimetic tissue for model systems [46][3]. Spheroids and organoids can create 3D tissue model systems. Still, they lack the vasculature, which is crucial for supplying oxygen and nutrients to cells and eliminating metabolic waste, a significant drawback in 3D microenvironments [46][3]. As an alternative, a scaffold that resembles the extracellular matrix (ECM) and features porous structures capable of retaining transcription factors, growth factors, vasculature, and cells is created using techniques such as 3D bioprinting, electrospinning, and solvent casting/particulate leaching (SCPL). A 3D model replicating tissue-specific conditions can aid drug testing and study intricate mechanisms in human development and disease progression, providing a deeper understanding of their significance [46].

Types of three-dimensional (3D) tissue models, each with unique characteristics and applications, are described in Table 1.1[46]:

Table 1.1 - Characteristics and Applications of different 3D Models.

3D models	Characteristics	Applications
Organoids	➢ Spherical structures formed by cell aggregation. ➢ Different cell types, such as stem cells and cancer cells, can be used to create them.	➢ Studies on cell activity. ➢ Research on medication reactions. ➢ Investigations into tumor biology [46][48].

	➢ They replicate the cellular architecture and milieu of real tissues. ➢ Offer improved cell-cell communication. ➢ Provide a more native design compared to traditional monolayer techniques [46][48].	
Hydrogel-Based Models	➢ Act as a supporting matrix for the development of cells. ➢ Can be customized to have specific mechanical properties. ➢ They enable the controlled release of growth agents [46].	➢ Used to make scaffolds for tissue engineering. ➢ Create 3D structures that resemble the extracellular matrix (ECM) [46].
Scaffold-Based Models	➢ Are three-dimensional constructs. ➢ Offer a framework for the attachment and development of cells. ➢ Techniques like electrospinning and 3D printing can be used to create them [46].	➢ Useful for applications in tissue engineering and regenerative medicine because they may be made to have mechanical and porosity characteristics [46].
Microfluidic Models (Organ-on-a-Chip)	➢ Living cells are integrated into microfluidic devices. ➢ The environment resembles an organ's physiological parameters. ➢ These models can study cell behavior in response to chemical gradients,	➢ Helpful for comprehending organ interactions. ➢ Useful for drug testing [46-49].

	mechanical stresses, and fluid flow [46-49].	
Bioprinted Models	➢ In 3D bioprinting, living cells and biomaterials are deposited layer by layer to construct sophisticated tissue architectures. ➢ This method allows precise control over the arrangement of cells and extracellular matrix elements in space. ➢ It creates tissues that closely mimic natural structures [46].	➢ Promising for transplantation. ➢ Useful in regenerative medicine [46].
Tumor Models	➢ Tumor spheroids and organoids are made from cancer cells. ➢ They are specific 3D models created to research cancer biology. ➢ These models provide a more physiologically appropriate setting [46][47].	➢ Understanding tumor growth. ➢ Studying metastasis. ➢ Investigating therapeutic responses [46][47].
Co-culture Models	➢ Different cell types are grown in the same three-dimensional space in co-culture systems. ➢ This technique allows for the study of cell connections and communication [46].	➢ Understanding tissue function. ➢ Investigating disease mechanisms [46].

The diversity of 3D models reflects the complexity of human tissues and the need for more accurate experimental systems in biomedical research. Each model type offers unique advantages for studying specific biological processes, disease mechanisms, and therapeutic

responses, making them invaluable tools in drug discovery, tissue engineering, and regenerative medicine.

1.10 3D Bioprinting

Bioprinting is a well-known and popular technique in the field of biofabrication [48]. The layer-by-layer deposition of cell-rich biomaterials in three dimensions according to a predefined shape is known as three-dimensional bioprinting [49]. Bioprinting is the use of computer-aided and additive manufacturing methods for the standardization and construction of living and non-living materials with a predetermined two-dimensional (2D) or 3D architecture to create bioengineered structures for regenerative medicine, pharmacology, and fundamental cell biology studies [48-51].

A key aspect that differentiates 3D bioprinting from traditional biofabrication approaches (such as pore leaching or gas foaming) is the possibility of incorporating biologically relevant molecules and cells with high spatial control at the exact moment of scaffold fabrication and depositing the biomaterial with microscopic precision [48][52].

Three phases are usually included in the manufacturing of 3D bioprinted human tissues: pre-processing, processing, and post-processing. The pre-processing stage is equivalent to creating a scaffold model for human cell culture and 3D bioprinting. The objective of the processing stage is to use 3D bioprinting to create the loaded architecture of 3D cells. Ultimately, the post-processing stage entails the synthesis of cell-filled constructs to fortify the creation of tissue constructs. [53].

The greatest feeding, oxygen supply, and waste management strategies must be used to maintain the cells' viability and functionality. Above all, cellular activity and the development of human tissues are greatly influenced by chemical and mechanical signals [49][56][57]. The ink formulation that enables the printing of cells and growth factors makes up the biomaterial that is printed, also known as bioink. Choosing the right bioink is crucial to a successful bioprinting process [49].

Even though there is a vast collection of biomaterials available, not all have the gelling qualities required to preserve the final printed structure's shape; instead, they require modifications to improve their mechanical strength and their chemical, physical, and biological characteristics. In some cases, photon activation by UV light in the presence of a photoinitiator or ion crosslinks in the presence of divalent cations are post-processing crosslinking mechanisms that stabilize bioinks [49]

1.10.1 Types of 3D bioprinting

The three primary technologies used in 3D bioprinting are extrusion (achieved by screw, piston, or pneumatic extrusion), inkjet (achieved by thermal or piezoelectric methods), and laser-assisted. These techniques rely on the way that bioinks, or biomaterials loaded with cells, are delivered. [49]

1.10.1.1 Extrusion-Based Bioprinting

Extrusion-based bioprinting (EBB) is a technique in which mechanical or pneumatic force is used to extrude bioink through a nozzle (Figure 1.3) [53]. This process prints cylindrical filaments in three-dimensional structures by combining an automated robotic extrusion system with a fluid-dispensing system. [68][69]. Compared to inkjet bioprinting, electrohydrodynamic bioprinting (EBB) has some clear benefits. It prints faster, reduces the risk of clogging, allows for printing materials that are less viscous, and can achieve higher cell densities [70-72]. However, it also causes shear stress in cells and has reduced fabrication resolution, which decreases printing fidelity [56][73]. A biomaterial appropriate for EBB needs to flow steadily until it deposits and quickly stabilizes after that [48]. Human tissues, including cardiac constructs with a high orientation index and blood-vessel-like geometries that facilitate the integration of engineered tissue with the host's vasculature, have been bioprinted using extrusion-based bioprinting [74-88].

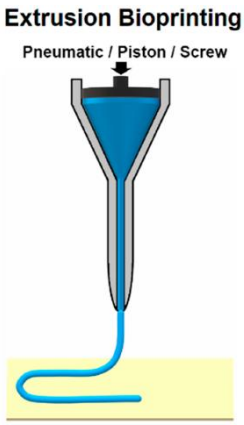

Figure 1.3 — A main type of bioprinting system: extrusion-based bioprinter. Sourced from [46]

1.10.1.2 Inkjet bioprinting

Also known as drop-on-demand or drop-on-demand bioprinting, it is a contactless method for 3D printing scaffolds and biomedical devices [56-58]. Piezoelectric inkjet, thermal

inkjet, and electrostatic inkjet bioprinting (Figure 1.4) are the three printing technologies that can be used to create bioink droplets. [59-61].

It allows the printing of cell-laden droplets at high resolution in microscale (10-75 μM) at low cost, fast fabrication, and high resolution [53][62-64]. On the other hand, drawbacks include poor cell density, droplet drying, restricted ability to create in three dimensions, and nozzle clogging. Extremely viscous bioinks are unsuitable for inkjet bioprinting, and bioink viscosity is a crucial parameter that needs to be regulated [58][62][65-67]. Because of their low viscosity, the 3D printed structures often have lower mechanical strength than the intended in vivo tissues [60].

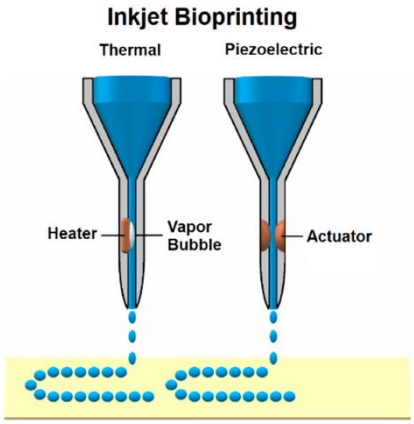

Figure 1.4 — A main type of bioprinting system: inkjet bioprinter. Sourced from [46]

1.10.1.3 Laser-based bioprinting

In laser-based bioprinting (Figure 1.5), cells are transferred from a source and pooled on a substrate. This process is also known as laser-guided direct or laser-induced cell printing. Because the refractive indices of cells and cell medium differ, this technique allows for the selective transfer of cells [53][57][66]. High-cell density bioprinting without clogging is possible with laser-based bioprinters since they are nozzle-free and can print various viscosities. Additionally, this method decreases cell stress and viability [53][58]. Laser-based bioprinting has been employed in biomedical applications, including the fabrication of human osteoprogenitor cells (HOP) and nano-hydroxyapatite (nHA) without modifying their properties, hence maintaining their viability, phenotypic, and proliferation, despite its more significant cost [53][81].

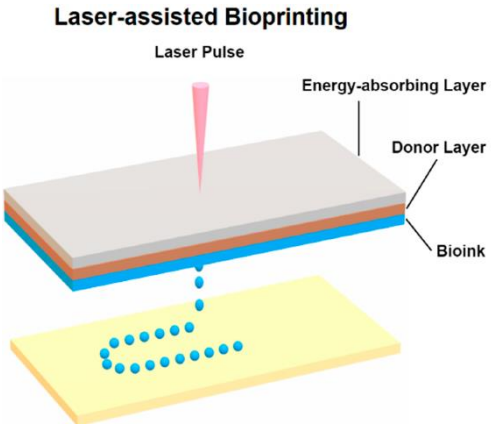

Figure 1.5 — A main type of bioprinting system: laser-based bioprinter. Sourced from [46]

1.10.1.4 Other types of bioprinting

A new technology called Reversible Incorporation of Suspended Hydrogels (FRESH) was recently used by Mirdamadi et al. [49] to achieve 3D bioprinting in addition to these three primary and well-known technologies [49]. Using an extrusion-based bioprinter that they had adapted for the study, the authors added alginate to a support bath that contained gelatin microparticles floating in a calcium chloride solution [49]. The resolution and low printing fidelity of extrusion-based printing can be overcome with the FRESH bioprinting technology. To completely cure the bioink, it must be extruded within a yield-stress support bath. The bath contains gelatin microparticles, which serve as a support bath using various cross-linking techniques to gel the various hydrogel types. Additionally, the bath supports embedded hydrogels, which, in traditional additive manufacturing processes, would collapse during printing and lock the bioink in place during extrusion. Volumetric patterning is possible since the support bath is liquified and removed after printing [49][79][80].

Suspended Layer Additive Manufacturing (SLAM), a stable hydrogel with low viscosity, was developed by Senior et al. by modifying the FRESH bioprinting technique. After removing the shear strain, they extruded bioinks onto an agarose gel, which restored its structural integrity. Next, the gel included a crosslinker, producing stable structures that were simple to remove [49].

Organ printing had previously been accomplished using microgel support baths; however, a novel method known as sacrificial writing on functional tissue (SWIFT) bioprints a sacrificial bioink inside a slurry support bath of cellular spheroids. Using iPSC-derived embryonic bodies, or organoids, tissue-specific organ building blocks were 3D printed by Skylar-Scott et al. to create a live matrix. When the sacrificial ink in the matrix is removed, perusable conduits and branching channels are formed. It isn't easy to control position in 3D space, however.

Innovative approaches that provide flexibility in regulating variables, including scaffold geometry, printing speed, needle gauge, extrusion pressure, and bioink composition, are being developed to address these issues [49].

1.11 Rheological and Mechanical Properties

Rheological characteristics significantly influence cell division and proliferation within the hydrogel matrix. The viscoelastic qualities stand out among these characteristics. The chosen bioinks' viscoelastic properties are crucial for maintaining the shape integrity of the printed structure, requiring more force when dispensing the bioink [82]. Bioprinting techniques like inkjet and extrusion can cause cell damage due to higher shear stress levels, requiring bioinks to be suitable for extrusion at stress levels that preserve cell integrity [82][83]. Bioinks for inkjet and extrusion-based bioprinting require non-Newtonian effects like strong shear-thinning quality to lower ink viscosity, facilitate flow through the nozzle, and maintain reversibility after printing. This reduces cell damage, keeps the material capacity to stack, and ensures printing fidelity [83][84-86].

To be suitable for extrusion-based bioprinting, the polymeric material must dissolve in a volatile solvent with a viscosity range of 30 to > $6x10^7$ MPa [87]. The storage (G') and loss (G'') moduli of bioinks are additional crucial characteristics. The storage modulus of a polymeric substance establishes its solid-like characteristics [88]. A high storage modulus of a polymer makes extrusion more challenging due to its difficulty in flow, but it also ensures a stable and accurate shape after printing. A low storage modulus produces a more liquid-like polymer that may leak from the nozzle [89]. Because they change inversely, a lower storage modulus also results in a more significant loss modulus. Conversely, a high storage modulus indicates a low loss modulus. Because of this, a polymeric material that balances both moduli is appropriate for 3D bioprinting. To be more precise, a polymer that has a storage modulus greater than its loss modulus is more suited for this purpose since it can maintain its shape without sacrificing its extrusion capabilities [88-90]. Bioinks with lower viscosities (between 10Pa and 10000Pa) and low storage modulus (<1500 Pa) showed more significant cell proliferation and a porous shape in comparison to materials with higher viscosities [82]. Furthermore, these factors also dictate the rate at which the polymer will degrade in response to mechanical force [89-90].

Maintaining a steady 3D network after printing is another essential characteristic of the bioinks. The crosslinking technique significantly influences Bioinks' stability, as it affects the development of reticulated networks, which can either develop irreversibly or reversibly after

printing [91]. Hydrogels are the most popular biomaterials for extrusion-based bioprinting since they form polymers that frequently exhibit essential bioink characteristics [92]. High shape fidelity is linked to yield stress, a non-Newtonian phenomenon found in colloidal gels, suspensions, and emulsions, a lower stress threshold at which solid-like materials deform plastically [93-95]. In addition to typically displaying viscoelastic behavior, materials used in bioinks can also show thixotropy, reversible, time-dependent isothermal decrease in the material's apparent viscosity when subjected to an increasing shear rate [95][96]. Because of their challenging nature, gel bioinks can exhibit both fluid and soft solid-like material qualities depending on the applied perturbations. The intricacy of these materials suggests that their rheology cannot be examined using the framework of Newtonian viscous fluids. The rheological behavior of optimal bioinks should include the following alternating steps in the printing process: gel behavior due to the dominance of elasticity over viscous (liquid-like) behavior before extrusion; structural break-up with liquid-like behavior prevailing during extrusion; complete structural build-up with a return to the original state upon deposition [97-100].

Mechanical qualities are crucial for creating mature and functional bioprinted cardiac constructions, as they should resemble native myocardium characteristics to facilitate synchronous beating, force production, and development [82].

Being a dynamic organ, the heart goes through constant cycles of contraction and relaxation. As a result, any material used in cardiac tissue engineering must have mechanical characteristics that perfectly mimic or enhance the environment of the original tissue. Young's Modulus (E), which gauges a material's stiffness, is one of the most essential mechanical parameters to consider. To maintain the elasticity necessary for regular heart function and to sustain contractility and cell-matrix interactions, the modulus of cardiac tissue must fall within a specific range. The stiffness of adult human cardiac tissues typically lies between 10 and 20 kPa (Young’s modulus end-systole) and between 200 and 500 kPa (Young’s modulus end-diastole); Hydrogels must be within this range to accurately replicate the physiological environment [101][106-108].

2

STATE OF THE ART

Cardiac tissue engineering is an emerging field of biomimetic scaffolds and cell-laden matrix products that help to facilitate the repairs of damaged cardiac tissues. As the heart can only regenerate naturally to a limited extent, functional scaffolds are essential for restoring mechanical, electrical, and biochemical functions. The progress toward recreating artificial models of cardiac tissue is an evolving field in cardiac tissue engineering. To do this, a biocompatible, mechanically sound and electrically conductive material will be required. This is where the utilization of hydrogels, in particular GelMA, has real potential alongside 2D nanomaterials like MXenes for developing a conducive biocompatible scaffold that emulates the intricate environment present within the native heart. Materials of this type have shown promise in constructing scaffolds that enhance the biological cues necessary for regenerating heart tissue and provide mechanical support.

Boularaoui et al. presented a significant advancement in 3D bioprinting, particularly for skeletal muscle tissue engineering. The authors focus on developing bioinks that combine GelMA with MXene nanosheets and gold nanoparticles to enhance the printability and biological properties of the resulting constructs. The research emphasizes using low-concentration GelMA hydrogels (≤5% w/v), which are biocompatible and allow for high cell viability, elongation, and migration. However, these hydrogels typically exhibit poor printability. By incorporating MXene nanosheets and gold nanoparticles, the authors achieved significant improvements in the electrical conductivity of the bioinks. This enhancement is crucial for the differentiation of encapsulated myoblasts and overall tissue functionality. The addition of these nanomaterials also improved the rheological properties of the bioinks, which is essential for maintaining shape fidelity during the printing process. The optimized bioinks demonstrated enhanced printability, particularly at lower temperatures (10 °C). The study reported a high cell viability

rate (97%) in the printed constructs, indicating that the bioinks support cell survival and promote myoblasts' differentiation into functional muscle tissue. The findings suggest that the developed nanocomposite bioinks represent a promising approach for creating 3D conductive tissue constructs with physiological relevance, paving the way for advancements in regenerative medicine and tissue engineering applications [103].

G. A. Asaro et al. synthesized conductive biohybrid scaffolds by incorporating 2D titanium carbide (MXene) into collagen-type I-based materials, improving electrical properties and mechanical performance up to native tissue. Among the key findings is the excellent biocompatibility of these MXene platforms, which results in enhanced proliferation and spread by fibroblasts with substantially limited bacterial attachment (specifically Staphylococcus aureus). When seeded with neonatal rat cardiomyocytes (nrCMs), human induced pluripotent stem cell-derived cardiomyocytes (iPSC-CMs) on these substrates exhibited significantly improved cell spreading and viability over a week relative to collagen controls. This work demonstrates the promise of MXene-based biohybrid platforms for cardiac tissue repair and suggests its potential utility in diverse biological applications in which electric conductivity is needed. In summary, these studies establish a direction for developing next-generation biomaterials that may regulate electrically sensitive cell maturation for regenerative therapy applications [115].

X. P. Li et al. showed that the addition of polydopamine-reduced graphene oxide (PDA-rGO) to Gelatin-Methacryloyl (GelMA) hydrogels results in a conductive, biocompatible matrix that can replicate some properties of the natural extracellular environment necessary for cardiac tissue engineering. This hybrid hydrogel enhances the mechanical stiffness and electrical conductivity required for CMs cell growth and function. We demonstrated that PDA-rGO improves CMs survival, adhesion, and proliferation and enhances synchronous beating behavior (critical to developing functional cardiac tissue). This novel method is designed to resemble heart tissue's in vivo extracellular matrix by enhancing critical electrical and mechanical properties for CMs development. Different concentrations of each reagent were tried to optimize the hydrogel composition. First, a 6% (w/v) GelMA concentration was chosen as the scaffold material for further study because it enabled an optimal balance between mechanical properties required for casting into square hydrogel substrates and cytocompatibility that would support engineered CMs construct generation. PDA-rGO (1 mg/mL was the optimal concentration). This amount improved electrical conductivity and mechanical stiffness, leading to considerably higher CMs viability, protein expression, and synchronous beating. To enhance UV crosslinking, 0.5% w/v LAP was included in the bioinks as a photoinitiator for excellent physical stability. These optimized amounts of GelMA, PDA-rGO, and LAP combined to form a hydrogel

facilitated the improved adhesion, retention, and maturation of cardiomyocytes on this hydrogel surface in response to external electrical stimuli. This advance demonstrates excellent potential as a scaffold for different applications in cardiac tissue engineering, disease modeling, and drug screening [117].

Since there is no recent work combining GelMA with MXenes for Cardiac tissue engineering, specifically for arrhythmia, these three papers were taken as pillars of this thesis work to help choose the best concentrations of each reagent (GelMA 6%(w/v), MXenes 0.5mg/ml, and LAP 0.5%(w/v)).

To address the challenge of arrhythmia, this project seeks to develop a physiologically relevant in vitro model of cardiac arrhythmia to facilitate drug development. This includes enhancing the maturity and functionality of cardiac tissue constructs, reproducing arrhythmic behaviors, and modeling diseases to provide insights into arrhythmia treatments. The objectives involve creating a conductive bioink, characterizing its properties, and subsequently conducting in vitro assays to ensure its biocompatibility and non-toxicity, ultimately leading to the development of the arrhythmic model.

3

MATERIALS AND METHODS

3.1 Materials

The materials used were gelatin (Sigma-Aldrich, Gel strength 300 g Bloom, type A from porcine skin, CAS number: 9000-70-8), phosphate buffer saline - PBS (made by me with salts purchased from Sigma-Aldrich), methacrylic anhydride (Sigma-Aldrich, contains 2,000 ppm topanol A as inhibitor, ≥94%, CAS number: 760-93-0), 14kDa dialysis membrane, filtered de-onized water. The following equipment was used: BioX6 CELLINK bioprinter (CELLINK, Sweden), 18G polymeric nozzles (CELLINK, Sweden), 3 ml bioprinting syringes (CELLINK, Sweden), and reusable glass material.

3.2 Synthesis of GelMA and GelMAX

Methacrylate gelatin was synthesized using a previously reported procedure (Figure 3.1) [18][102].

In summary, 20 ml of PBS and 2.0 g of porcine gelatin were dissolved while stirring at 50 ºC. 8 ml of methacrylic anhydride (0.5 ml/s) was added drop by drop until the solution was noticeably homogenous and 20% (w/v) was reached. For one hour, the mixture was stirred at the same temperature. Additional PBS was used to create five dilutions (5x20 ml) to sate the reaction. The resultant solution was stirred at 60 ºC for an extra hour. To make a cottony crystalline foam, the solution was dialyzed for 4 days at 50/60ºC, frozen for an additional night, and finally placed in a freeze dryer for a minimum of 4 days. In the preparation of GelMAX,

which consists of GelMA with the incorporation of MXenes during the synthesis, a solution was created using the initial 20 mL of PBS to facilitate the integration of the MXenes into the matrix.

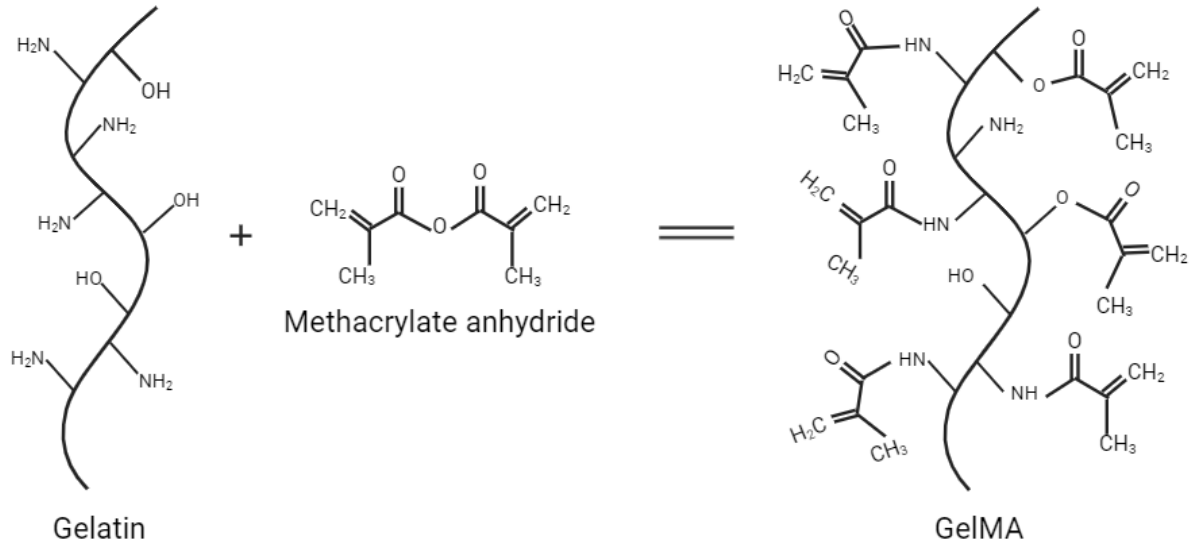

Figure 3.1 — The process of methacrylate anhydride and gelatin combine chemically to form GelMA. Adapted from [116].

3.3 Preparation of Bioinks

3 different types of bioinks have been developed:

- 6% (w/v) GelMA, 0.5% (w/v) LAP: GelMA;
- 6% (w/v) GelMA, 0.5mg/ml MXenes, 0.5% (w/v) LAP: GelMA-MX;
- 6% (w/v) GelMAX, 0.5% (w/v) LAP: GelMAX.

The synthesis of the different groups was carried out similarly. First, GelMA was dissolved in ultrapure water at 50ºC, resulting in a final concentration of 6% (w/v). After the solution was homogenized, the LAP photoinitiator was added in a dark environment and homogenized for 1 hour. Next, the nanoparticles (NPs) were incorporated into the GelMA mixture, with a waiting period of approximately 30 minutes to ensure that the NPs were evenly distributed throughout the GelMA solution. The LAP photoinitiator was added again in a dark environment and allowed to homogenize for another hour, Figure 3.2. For the GelMAX group, since the NPs have been introduced previously, the LAP photoinitiator is added to the homogenized GelMAX in a dark environment and allowed to mix for 1 hour, Figure 3.2.

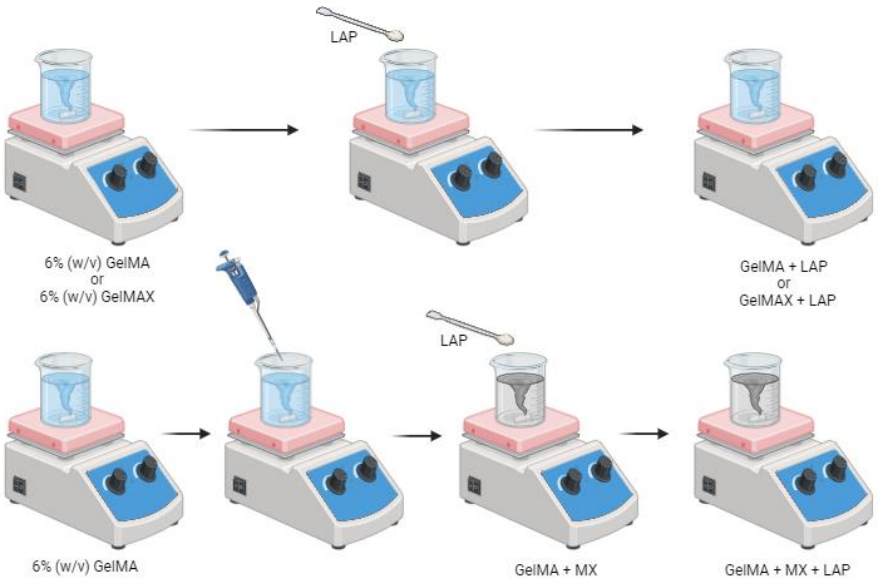

Figure 3.2 — Preparation of the different bioinks.

3.4 Transfer of bioinks to the printing syringe

Once prepared, the bioinks should be stored in light-protected bottles in the refrigerator. The day before printing, remove the vial from the refrigerator and gently warm it in a dark environment. Using a clean syringe, transfer the desired bioink from the vial to the syringe, ensuring it remains protected from light. If the room temperature is below 23/24ºC, the syringe can be kept at room temperature. However, if the temperature exceeds 23/24ºC, it is recommended to store the syringe in the refrigerator, Figure 3.3.

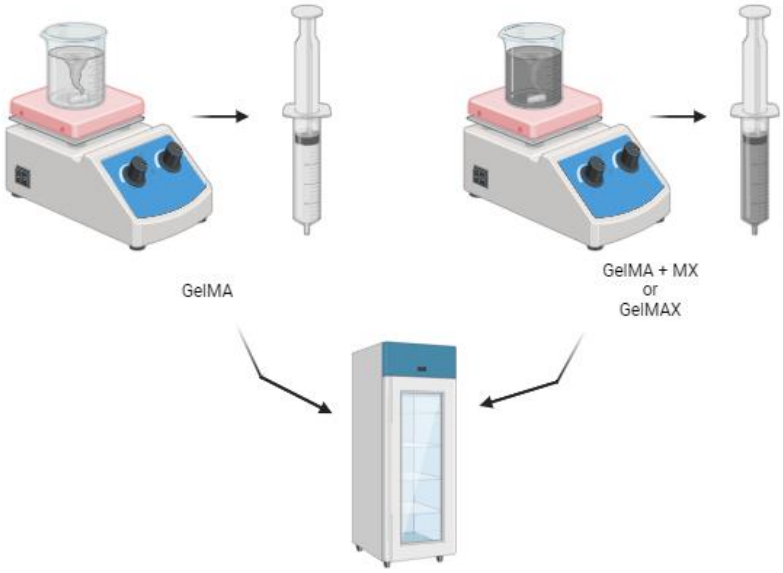

Figure 3.3 — Transferring the bioinks to the syringe and storage in a refrigerator.

3.5 MXenes Solution

Initially, 76 mM of LiF was dissolved in 30 mL of 6 M HCl solution. This step involves continuous stirring for 10 minutes. After the LiF is completely dissolved, 1.2 g of Ti_3AlC_2 powder is added to the mixture solution. This powder contains titanium, aluminum, and carbon. The mixture is then stirred at 45 °C for 40 hours. During this time, the aluminum element in the Ti_3AlC_2 powder is etched away. After the etching process, the suspension is transferred to a centrifuge tube and centrifuged. The purpose of this step is to separate the MXene material from the remaining solution. The precipitate is washed several times with deionized (DI) water. Each washing step involves handshaking and centrifugation at 3000 rpm for 5 minutes. The washing process is repeated until the pH of the solution reaches a desired level. Once the washing is complete, the precipitate (which should now contain the MXene material) is dried at 40 °C for 24 hours in a vacuum. After drying, the MXene material is obtained in the form of a black powder. To disperse MXenes, it is mixed with a certain amount of a polar solvent (water) and then sonicated for 1 hour. Sonication helps to disperse the MXene powder evenly in the solvent. This protocol was carried out by someone with expertise within the field.

3.6 Characterization of the Bioinks

3.6.1 NMR Spectra - Quantification of the degree of methacrylation (DM) of GelMA

The methacrylation of gelatin was shown using 1 H-NMR spectroscopy. 30 mg GelMA samples were analyzed after being dissolved in 300 µL of deuterium oxide. High-resolution proton NMR spectra at 500 MHz were acquired using a Bruker Avance 500 spectrometer. Bruker Topspin 4.1.4 was the data processing software that was utilized. The Degree of Methacrylation refers to the proportion of the amino groups (lysine and hydroxylysine) in gelatin that is changed in GelMA. To measure the DM using 1 H-NMR, the spectra were normalized to the phenylalanine signal (6.9–7.5 ppm), which reflects the gelatin concentration. The lysine methylene signals (2.8–2.95 ppm) of the gelatin and GelMA spectra were then integrated to yield the areas [A(lysine methylene of non-modified gelatin) and A(lysine methylene of GelMA)]. Equation 1 was used to determine the DM of the different GelMA batches.

$$DM_{NMR(\%)}=\left(1-\frac{A(lysine\ methylene\ of\ GelMA)}{A(lysine\ methylene\ of\ non-modified\ gelatin}\right)\times 100 \quad (1)$$

The 1H-NMR spectrums were conducted by someone with expertise within the field.

3.6.2 Rheological Tests

Using a plate-to-plate 25mm diameter geometry with a 1 mm gap and an Anton Paar MCR 502 modular compact rheometer, the rheological characteristics of the non-crosslinked bioinks were assessed at 10°C. Thixotropy, strain sweep with dynamic amplitude, stress sweep with dynamic amplitude, and steady-shear viscosity were among the tests conducted. Shear viscosity measurements were made between 0.001 and 1000 s-1. To evaluate thixotropy, time-dependent shear rate data were employed. Every sample experienced three distinct shear rate intervals: 0.1 [1/s] from 10 to 200 seconds, 100 [1/s] from 210 to 500 seconds, and 0.1 [1/s] from 510 to 700 seconds. These intervals served to test the material's capacity to regain viscosity as well as its reaction to varying shear rates over time. Dynamic stress-sweep experiments, employing a stress range from 0.1 to 1000 Pa at an angular frequency of 1 rad/s, and strain-sweep experiments with a strain range from 0,1 to 1000 % of deformation at a constant angular frequency of 1 rad/s, were performed to access the viscoelastic properties. The rheology measurements were conducted by someone with expertise within the field.

3.6.3 3D Bioprinting

A CELLINK Bio X 6 printer was used for the 3D printing procedure. The printer program's software was used to design the structure. A preview of the 3D models used is shown in Figure A.1. The Results section explains the various printing parameters that were investigated. After filling a 3 mL syringe with bioink and printing each layer of the structures on a petri dish, they were subjected to UV light. The stiffness of the structures was measured with a spatula to determine if the crosslinking had occurred. After that, a phone camera was used to take pictures of the hydrogels.

3.6.3.1 Printability and Printing Accuracy

Every bioprinting experiment was evaluated for printability using a CELLINK bioprinter. Although the initial experiments were intended to be conducted at cell incubation temperature (37 ºC), this was not feasible due to limitations in the system, therefore they were instead carried out at room temperature (22/24 ºC) in the cold months and 10 ºC in warmer months. The selected nozzle gauge 18G (Inner Diameter=0.84 mm) was used in experiments, and printing parameters (printing speed and flow) were tuned. A petri dish was used as the printing surface for the printability experiments.

Using Bio X6's CELLINK software, a single 2x2 (1mmx1mm) monolayer square net was created to test the accuracy of printing the ribbon thickness in a single layer. The proof of concept used in this test is displayed in Figure A.1. Following the printing of a material layer, the dimensions and printing parameters were computed using the ImageJ software. The wire's width and length were measured multiple times before being averaged.

3.6.4 Electrical Characterization of the Bioinks

The electrical characterization was conducted through an Inlab 751-4 mm electrode (METTLER TOLEDO). First, the electrode was calibrated with two conductivity standard solutions: 12.88 mS/cm and 1413 µS/cm. Once calibrated, the measures were registered for the samples when at room temperature.

3.7 Characterization of the Hydrogels

3.7.1 Swelling

For the swelling study, the crosslinking was made with a nail oven, to simulate as possible the way was going to be carried out in Section 3.8.1. Following the measurement and recording of the hydrated scaffold's initial weight, each sample was immersed in PBS at room temperature and then at 37 ºC. Following submersion, the weight of the submerged samples at room temperature was measured after 10 minutes, on the 1st, 3rd, and 7th day. After the samples were at room temperature, they were placed at 37 ºC, to simulate the cell culture environment. The weight was measured on the 1st and 2nd days after being at 37ºC. If there were any swelling, it would be most noticeable these days, as the hydrogels swell the most during this period. However, these findings will be discussed in section 4.

The Swelling is calculated as in equation (2), getting the relative percentage change:

$$\text{Relative Change (\%)} = \frac{Value\ at\ Time\ Point - Initial\ value\ (0min)}{Initial\ Value\ (0min)} \times 100 \qquad (2)$$

3.7.2 Scanning Electron Microscopy (SEM)

The samples were synthesized as explained in section 3.2 and printed as explained in section 3.6.3, dried at the desiccator with vacuum at 24 ºC, and were cut. Then they were put on the setup and coated with carbon before being examined under a Hitachi Regulus 8220 Series Scanning Electron Microscope (SEM) operated at an accelerating voltage of 3kV and

using the secondary electrons detector. The Images were conducted by someone with expertise within the field.

3.7.3 Atomic Force Microscopy (AFM)

As a result, GelMA, GelMA+MX, and GelMAX were the three groups on which the analysis was conducted. During the curve acquisition process, the samples subjected to atomic force microscopy (AFM) measurements were initially immobilized within a fluid cell and kept submerged in MilliQ water, Figure A.2. Using an Asylum Research MFP-3D Standalone AFM system (Oxford Instruments, UK), pre-calibrated nitride AFM probes with a 5 µm tip radius (SAA-SPH-5UM; Bruker, USA) were employed. Each sample has at least 392 force-displacement curves created in at least three distinct locations. Young's modulus, which was calculated by applying Hertz's contact model for spherical indenters to evaluate the retraction curve, indicates the elasticity of the material. The AFM measurements were conducted by someone with expertise within the field.

3.8 Cellular Assays

3.8.1 Cell Culture

Human induced pluripotent stem cell-derived cardiomyocytes were embedded in the scaffolds. The bioink samples were mixed with cells; in each well 200 µL of the bioink with approximately 2.5 x 10^5 cells per construct was placed. After placing them, we proceed with the crosslinking using a nail oven for 60 seconds and 2 minutes. Once the constructs were crosslinked, 2ml and 1ml of medium with antibiotic were placed. The medium was changed every two days until day 7.

3.8.2 Live/Dead Staining

On day 7, the cell viability was assessed using a viability/toxicity kit from Invitrogen by Thermo Fisher Scientific. For each well, 10 µL of ethidium homodimer-1 and 2.5 µL of calcein AM were mixed with 5 ml of PBS, and then 200 µL of this mixture was added. The images of the cells were captured using a microscope from Carl Zeiss Microscopy GmbH, 30 minutes after the viability assay was performed. Cell viability was calculated using equation 3, where Alc represents the area of live cells and Adc represents the area of dead cells. In a separate cell culture, 10 µL of ethidium homodimer-1 and 20 µL of calcein AM were mixed with 5 ml of PBS.

Then, 500 µL of this mixture was added per well, and the images were captured 30 minutes after the viability assay was performed. This was carried out at Nova Medical School by someone with expertise in the field.

$$\text{Cell Viability (\%)} = \frac{\text{Alc}}{\text{Adc} + \text{Alc}} \times 100\% \qquad (3)$$

3.8.3 Presto Blue Assay

To assess the metabolic activity of cells, the Presto Blue assay was used. Each well-received 50 µL of the Invitrogen by Thermo Fisher Scientific Cell Viability Reagent was applied and incubated for 15 minutes at 37 °C. The medium was 500 µL in each well. Next, 150 µL was removed from every well and placed in each well of a 96-well plate, ensuring that each sample was duplicated. Using Softmax Pro software, the 96-well plate was placed in a SpectraMax i3x Multi-Mode Microplate Reader to measure fluorescence. Following fluorescence measurement, the medium was replaced and incubated at 37 °C. On day seven, the assay was run on two samples with cells from each group and one sample without cells. This was carried out at Nova Medical School by someone with expertise in the field.

3.8.4 Immunofluorescence

The sample was fixed in 4% (w/v) paraformaldehyde. Subsequently, the sample was rinsed with a 0.1% (w/v) Triton X-100 solution for permeabilization. 100 µL of a solution with 1 ml of PBS, 200 nM of Phalloidin Alexa 555, and 1 µg/ml of DAPI was placed in the scaffold well, followed by another three washes in PBS. The confocal microscope model Zeiss was used for the images. The Images were conducted by someone with expertise within the field.

3.8.5 Scanning Electron Microscopy (SEM) after Cell Culture

SEM imaging of the samples was utilized to study cell morphology. For 30 minutes, they were fixed in a 4% (w/v) paraformaldehyde solution. After that, it was Immersed two times in a PBS bath. The samples were dehydrated using a graduated ethanol bath, which included 50% ethanol at first, 70% ethanol at next, 80% ethanol at next, 90% ethanol at last, and 100% ethanol at last. Waited 5 minutes between each bath. The 100% ethanol bath was made 2 times; the second time was refrigerated it overnight. Following room temperature drying, the samples were sliced and placed on a vacuum desiccator, then subjected to a carbon coating and

scrutinized using a Hitachi Regulus 8220 Series SEM. The Images were conducted by someone with expertise within the field.

3.8.6 Atomic Force Microscopy (AFM) after Cell Culture

The synthesis of the samples followed the instructions in section 3.2 also but went to cell culture as in section 3.8.1 before AFM measurements. As a result, GelMA+Cells, GelMA+MX+Cells, and GelMAX+Cells were the three groups on which the analysis was conducted. The rest was carried out the same way as in section 3.7.3. The AFM measurements were conducted by someone with expertise within the field.

3.8.7 Statistical Analysis

All results are presented as mean ± standard deviation. Statistical analysis was performed with the software GraphPad Prism 9.5.1. The values were compared using either a two-way ANOVA or a one-way ANOVA with Tukey's multiple comparisons test. The level of significance accepted was $p<0.05$.

4

RESULTS AND DISCUSSION

4.1 Quantification of the degree of methacrylation (DM) of GelMA - NMR Spectrums

The material was created by reacting methacrylic anhydride with porcine gelatin. The extent of conversion of free amine groups in the initial material was determined by 1H-NMR analysis, confirming the successful methacrylation. The 1H-NMR spectra of unmodified porcine gelatin, GelMA, and GelMAX (see Figure A.3) show new signals detected between 5.3 and 6.4 ppm, indicating the presence of the acrylic protons of the methacrylic functions. The rates of derivatization are 81.35%, 61%, and 86.44% (as shown in Figure A.3 B1, B2, and C), based on the reduction in the integration of the methylene lysine signal at 2.9 ppm, normalized with the phenylalanine protons. Findings are consistent with those of Hoch et al.[18][102]. Figure A.3 shows that the novel approach of integrating the MXenes nanoparticles when the synthesis is occurring does not affect the methylation process.

These hydrogels maintain gelatin's enzymatic degradability, thermosensitivity, and cell adhesion domains thanks to the functionalization of its primary amine groups [102].

4.2 Bioinks Characterization

4.2.1 Rheological Testing

The scientific literature covers a variety of methods for determining a bioink's printability, ranging from straightforward observations to quantification. The initial assessment of bioink printability includes fiber formation and layer stacking. However, rheological measurements and characterization result in more comprehensive information. This work evaluated bioinks' shear-thinning and viscoelastic behaviors and their recoverability after low–high strain levels, as shown in Figure 4.1 and Figure 4.2.

These experiments were conducted at 10ºC on each group listed in section 3.3.

Viscosity is a measure of how quickly a fluid's layers move about one another. To see how the fluid's resistance to flow varies when it is sheared more quickly, see Figure 4.1A graph, which displays viscosity against shear rate. All three have shear-thinning behavior, a requirement for 3D printing. Even though GelMAX+LAP exhibits a relatively high viscosity compared with the other two samples that exhibit shear-thinning behavior as well, they have a flow more easily right out of the nozzle because of their significantly lower viscosity than the GelMAX+LAP. Gels and pastes frequently exhibit shear-thinning, which is the ability to reduce viscosity when applied or mixed and increase handleability. [103]

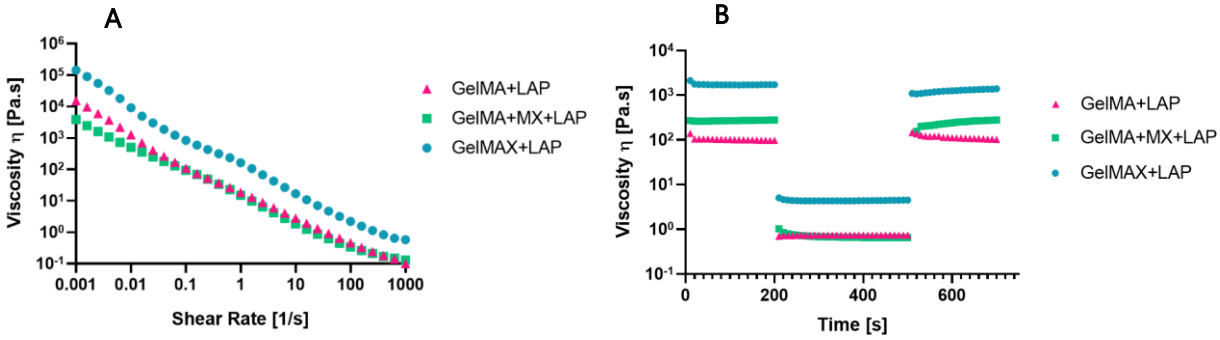

Figure 4.1 — Rheological characterization of GelMA, GelMA+MX, and GelMAX Bioinks. (A) Viscosity graph and (B) Thixotropy graph

Thixotropy is the property of some gels or fluids that, while thick (viscous) under ordinary circumstances, gradually lose their viscosity when disturbed or subjected to other stresses. In Figure 4.1B viscosity, a gauge of a fluid's resistance to flow, is plotted for three separate samples over time. All the samples appear to have a rapid viscosity recovery after a high cutting rate. This test shows that the material recovers its molecular structure quickly to hold the next layer that will be deposited on it after printing. This can be seen here with the viscosity recovery time. The viscosities are comparatively steady over time, indicating that these materials exhibit stable thixotropic behavior that is, their resistance to flow does not alter significantly over time. This means good performance by the bioinks when used to print since all showed a quick ability to recover after applying pressure to print. [103]

Strain Sweep quantifies how material structure (G' and G" moduli) responds to increasing strain or deformation. There are two components of the way the material behaves: how elastic or solid it is (represented by Storage Modulus (G')) and how viscous or liquid-like it is represented by Loss Modulus(G"). As the value of G' drops below G'', this crossing point reflects where the material behaves more like a liquid than a solid (Figure 4.2A and B). All the samples

exhibit similar behavior. The GelMAX+LAP shows an earlier G'=G″ crossover, but all maintain the required elastic structure for 3D printing (Fig. 4.3 A) [103].

Stress Sweep is where stress (applied force) varies, and the response is observed. Figure 4.2 B GelMAX+LAP sustains high G' values under a flow curve up to even higher stresses, which indicate solid-like properties that Improve with increasing forces applied in the stress region of the yield point. GelMA+LAP and GelMA+MX+LAP have lower G′ and G″, thus indicating that these samples begin to flow or degrade when deformed under load. Yield stress, the point where G'=G'', is a crucial aspect of bioinks since it is the point at which the material is thick enough to sustain suspended cells, while above that stress, it will behave as a liquid flow [103]. The addition of MXene increased the yield stress of GelMA, and the highest yield strength among the bioinks was observed for the bioink with MXene, indicating better filament production and retention. However, the highest yield stress is for GelMAX+LAP.

All tests indicate that GelMAX+LAP acts appreciably tougher and more solid-like, therefore possessing superior resistance against flowability and deformation than the other samples. At the state of stress, GelMA+LAP and GelMA+MX+LAP show less resistance to flow and deformation, so these states are more like liquid. Besides every bioink print well, the one that was easier to handle when printing was the GelMA+MX+LAP, as can be seen in the next section, (4.2.2).

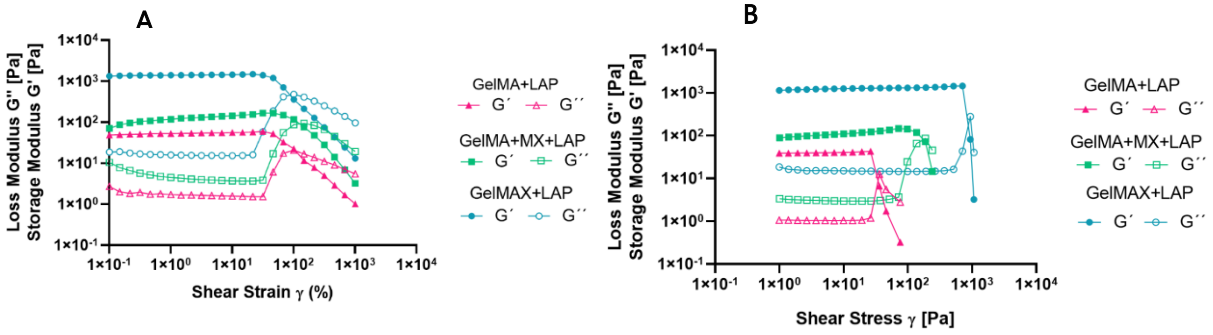

Figure 4.2 — Rheological characterization of GelMA, GelMA+MX, and GelMAX Bioinks. (A) Strain Sweep graph and (B) Stress Sweep graph

4.2.2 Printability and Printing Accuracy

A 3 ml syringe of each sample was produced to carry out these tests. As is well known, GelMA is a temperature-sensitive polymer. In the cold months, the bioinks became more viscous at room temperature, behaving like gels. However, in warmer months, the same bioinks remained liquid at the same room temperature. This highlights GelMA's sensitivity to

environmental conditions, affecting its gelation behavior. It was necessary to adjust the temperature using a proper chamber and a tip with cooling capacity to enable printing. In this case, a printability temperature of 10ºC was found to be consistent with the research by S. Boularaoui et al.[103]. To speed up the process of reaching the desired temperature of 10ºC, the syringe filled with the bioink was placed in the fridge the day before it was to be used. This step was necessary because, without cooling, the bioink would be too liquid, and even light pressure would cause it to flow out of the syringe, making printing difficult. Pressure was the only parameter adjusted during the process, while other settings remained constant: layer

Figure 4.3 — Design printed with the 3 different bioinks; Top view of 3D printed grids; The image on the left is GelMA+LAP; The middle image is GelMA+MX; The image on the right is GelMAX+LAP

height 0.84 mm, first layer height at 100%, grid infill pattern, 25% infill density, 18-gauge nozzle, print speed of 5.0 mm/s, UV wavelength 405 nm, 60 seconds of exposure time per layer. Three layers were printed for each sample.

The optimal pressure ranges found were:

- GelMA: 80kPa-90kPa. Starting at 80kPa, the pressure gradually decreased over time, requiring adjustments to maintain the flow.

- GelMA+MX: 70-80kPa, slightly lower than GelMA due to differences in viscosity.

- GelMAX: 100-115kPa, requiring higher pressure because of its more solid-like properties.

These results align with the rheology data, where GelMAX presents a more solid-like behavior, and the other bioinks present a liquid-like behavior.

Figure 4.3 shows that for the three bioinks, viscosity and crosslinking rate are ideal for the nozzle size and printing conditions, as seen by its excellent printability, which formed straight grid lines with little spreading. In the GelMA+MX, the clusters of MXenes show bioink heterogeneity; in GelMAX, the clusters of MXenes don't exist; the sample is homogeneous. The

Image of GelMAX was taken days after being printed, showing an aspect of dryness, but when printed, it was as bright and soft as the others.

Regarding printing accuracy, using Image J, it was possible to confirm that the angles were 90º and that the square's length and width were very close to the one in the design (1x1 cm). For GelMA, it was 1.06 cm ± 0.03; for GelMA+MX, it was 1.04 cm ± 0.06; and for GelMAX, it was 1.05 cm ± 0.05.

Ng et al. classified the final printing results into three categories: incomplete printing (discontinuous filaments), ideal printing parameters (desired outcome), and excessive material deposition (fused filaments, closed pores). Studies have shown that printing conditions leading to broken or discontinuous filaments are considered poor printability, as they can cause filament breakage [113]. With these, it can be concluded that the bioinks, as shown in Figure 4.3, have good printability since they present the desired design and maintain the structure after printing and UV curing.

4.2.3 Electrical Characterization

Tissues like muscle, neurons, lungs, and cardiac tissues have low electrical conductivity. Purkinje fibers help reduce electrical conduction in the native myocardium. The conductivity values of these tissues range between 0.03 and 0.6 S/m, the exact conductivity value for the myocardium is 0.1 S/m [110-112].

To conduct these tests, 3 ml of each sample was prepared, as in section 3.3. Despite our efforts to control the laboratory temperature, the bioinks remained liquid at room temperature. Figure 4.4 shows that all three bioinks are in the range of the native tissues with low electrical conductivity, indicating that all are suited for cardiac tissue engineering. Furthermore, the one that suits the best is the GelMAX group because the native myocardium's direct current conductivity is 0.1 S/m [112], and the GelMAX presents the conductivity more closely to this value. The conductivity of GelMAX may be affected by its slightly higher viscosity compared to the other samples when measuring conductivity at room temperature. Additionally, the other samples (GelMA and GelMA+MX) are completely liquid when measuring conductivity at room temperature, indicating that incorporating MXenes into the synthesis of GelMA increases its viscosity. The more viscous it is, the closer it is to the conductivity of the myocardium.

The GelMA+MX group may still be suitable for cardiac tissue engineering despite having a conductivity higher than 0.1 S/m. The higher conductivity may be due to the bioink being liquid at the measurement time. Additionally, the heterogeneously distributed MXenes

between the porous plates of the electrode could have led to a more significant accumulation in certain areas, thereby increasing the measured conductivity.

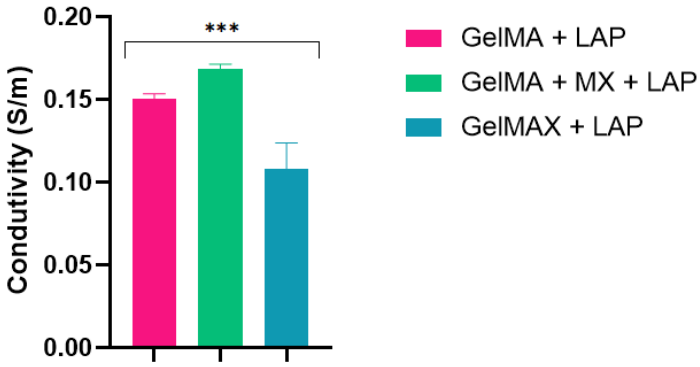

Figure 4.4 — Graph of conductivity of the Bioinks in the study, GelMA, GelMA+MX and GelMAX, *** p<0.0006

Comparing the two bioinks that were liquid (GelMA and GelMA+MX) when conductivity was measured with the electrode, MXenes effectively improved the conductive properties of GelMA without MXenes. The GelMA+MX formulation is more promising for reproducing the electrical properties of native heart tissue than the GelMA.

It would be imperative in the future to conduct conductivity tests after these are cross-linked to see if there was any change in the conductivity caused by the crosslinking and at 37ºC to see if there is any change in conductivity when the hydrogel is in a cell culture environment.

4.3 Hydrogels Characterization

4.3.1 Swelling

These tests were carried out to simulate the cellular environment and evaluate the swelling behavior of the hydrogels. The first cell test reflected a high swelling capacity of the hydrogel (Figure 4.5), which is why pre-cell swelling tests were carried out in the second cell test to prove the hydrogel's retention effectiveness. The UV lamp (365 nm+405 nm) was used for the swelling tests to be the most similar to cell culture since the bioprinter couldn't be taken to the facility where the cell culture was carried out.

To see what was causing the swelling, the following parameters were considered: temperature (room temperature and 37 ºC) and time (60 s and 99 s) of exposure to the UV lamp (photocrosslinking) since the UV lamp being used was not the one that was supposed to be (UV lamp from the bioprinter - 405 nm). At room temperature, the hydrogel was submerged in PBS over 7 days, and the weight was registered at 10 min after being immersed in PBS on

Figure 4.5 — First Cell Culture; The samples with a yellow tone color are the group of GelMA+LAP+Cells; The other samples with black dots are the group of GelMA+MX+LAP+Cells; Both were exposed for 60s.

days 3 and 7 (Figure 4.6). These time points were considered because, in a cell culture environment, the medium was changed with that frequency up to day seven (on the 3rd and 7th days). The measurements were taken at 10 minutes and 1 day because the anticipated behavior of a hydrogel is to swell the most and reach its maximum capacity within the first few minutes or hours. The total capacity can then be seen because the weight typically stabilizes. For better

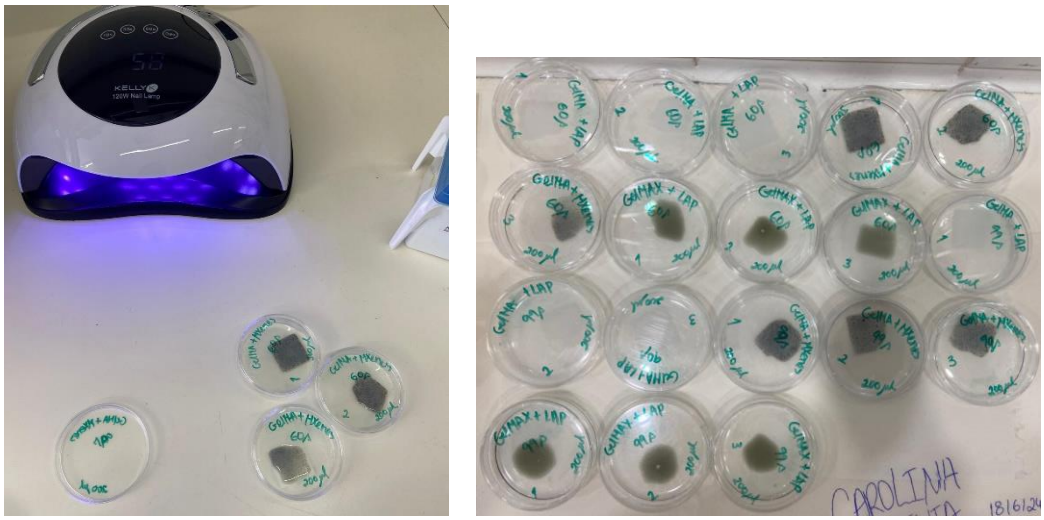

Figure 4.6 — On the left the UV lamp crosslinking the samples; One the right all the samples that were carried on the swelling test.

handling of the samples, they were placed on coverslips before exposure to UV light.

Swelling is crucial in tissue engineering, improving cell infiltration, pore size, and porosity. The physical properties of the hydrogels were assessed through expansion ratios, as shown in Figure 4.7 and Figure 4.8. GelMA+MX and GelMAX show the highest swelling due to their hydrophilic nature and large surface area facilitated by functional groups that increase water entry into the construction. The inclusion of nanomaterials in the gels can increase the osmolarity, resulting in higher osmotic pressure and attracting more water molecules.

Both Figure 4.7 and Figure 4.8 illustrate that none of the groups has a high swelling compared to its initial state at room temperature, which may be due to the handling of the coverslips and the drying of excess PBS for weighing. Some of the coverslips broke at the corners, which reduced their final weight. The weight of the coverslip without hydrogel was subtracted from the one measured, even with them broken, to make the calculations. The corners were the only places without samples to avoid damaging them. However, when handling the

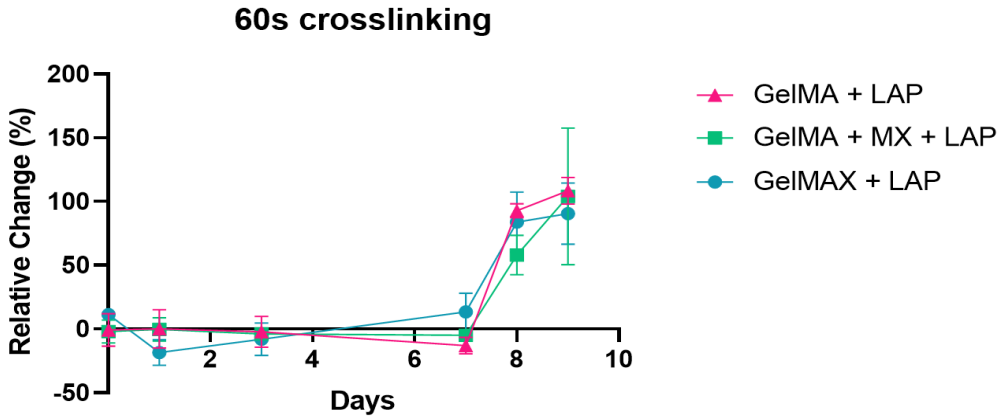

Figure 4.7 — Percentage of relative change in weight at room temperature (0 day - 7th day) in the groups with a 60 s exposure time to the UV lamp; 37ºC (7th day - 9th day)

tweezers, the absence of these corners caused small fragments of the samples to accidentally be removed by the fine tips of the tweezers. One factor that impacted the weight was the challenge of achieving uniform drying of the surface coverslip without causing any damage to the hydrogels. It can be inferred that measurements would be more precise at room temperature if there were no errors, and if the swelling did not occur or remained stable at a lower weight. On the 7th day, when the samples are exposed to a temperature of 37 ºC, we observe a significant difference in swelling. This temperature increase replicates the conditions of the human body, leading to increased water absorption. In Figure 4.7, GelMA+MX exhibits more linear swelling compared to the other groups, where swelling is non-linear. The substantial difference in weight is particularly noticeable at 37 °C. We hypothesize that these changes are due to gel network alterations and water interactions. This includes the disruption of some intra- and intermolecular interactions within the gelatin matrix, changes in network density, and the amount of crosslinking. When the polymer chains are more flexible and loosely packed, there is more room for the gel to expand and absorb water. One possible explanation for the weight gain in the samples at 37 °C compared to the samples at room temperature is that when the samples were weighed, it was noticeable that they detached from the coverslip, making it challenging to grab them and weigh them accurately. In order to solve this issue, we used a small spoon to assist in picking up the swollen sample. This allowed us to weigh a bit of water

with the sample, as it was impossible to dry it without damaging or completely ruining the sample.In Figure 4.8, swelling increases significantly, particularly after being placed at 37°C. GelMA+MX absorbs a significant amount of water compared to its crosslinking time of 60 seconds. GelMAX absorbs water but not as much as GelMA+MX. GelMA swells less than the other two, indicating it is more stable under these circumstances. Regarding other studies published, the expected behavior is to swell less with the increase of exposure time to UV light [104], which does not happen with the 99 s of exposure for GelMA+MX but happens to GelMAX and GelMA. Comparing the graphs of 99 s with the 60 s, it is visible that there was a decrease in swelling of the GelMAX and GelMA+MX, but this not only due to the density of crosslinking but also since the samples also detached from the coverslip and when handled to weight them one of them broke trying to take It out, and the others that stayed intact when weighted, water

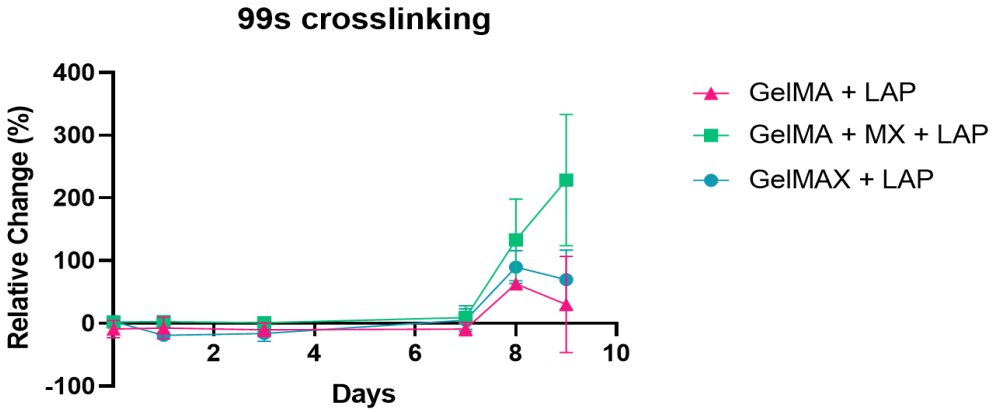

Figure 4.8 — Percentage of relative change in weight at room temperature (0 day - 7th day) in the groups with a 99s exposure time to the UV lamp; 37ºC (7th day - 9th day)

was weighted with them because It wasn't possible to dry properly like explored in the 60s samples at 37ºC.

It would be beneficial to repeat the swelling tests with a lamp with only one wavelength because it can be more efficient than using one with a combination of wavelengths. It cannot be efficient in crosslinking all the networks because when printing in the bioprinter and using only one type of wavelength, the resulting structure has more of a hydrogel texture than the other. The sample crosslinked with the combinations of wavelength is softer and always has around the structure some water, which can be residues of GelMA and LAP that did not polymerize.

Other times of UV exposure were tested for 2, 3, and 4 minutes with the nail lamp, all incubated at 37ºC to simulate where they swell the most in the previous tests because they would be used in a cell culture environment. These were qualitative tests because the time was

insufficient to register things properly, and the hydrogels did not have the same shape, initial weight, and height. The tests were conducted to determine which would best suit the second experiment involving cell culture. Figure A.4 represents some of the groups in the study, and the hydrogels did not show evident swell from day 1 to day 2. The hydrogels seemed more stable with high crosslinking times, as demonstrated by Shie et al. [101].

4.3.2 Scanning Electron Microscopy (SEM)

SEM was used to analyze the morphology of scaffolds. The scaffolds were dehydrated and sliced for this purpose. Figure 4.9 illustrates the cross-sections of each hydrogel. In Figure 4.9A, there are numerous interconnected pores, which give it an uneven and rough morphology. This structure may indicate good porosity, which is necessary for cell attachment and nutrition delivery in biological applications.

In Figure 4.9B can be seen the presence of some porous and verify that the presence of the MXenes doesn't alter the structure already established by the GelMA and LAP (Figure 4.9 A); this probably happens because the MXenes are in clusters. The surface is more complex and may indicate the presence of larger pore-like structures and possibly a more layered or

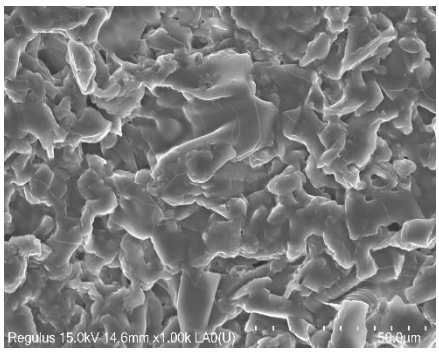

A - SEM image of a sample of GelMA+LAP

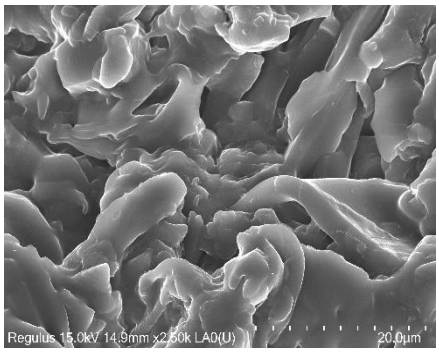

B - SEM image of a sample of GelMA+MX+LAP

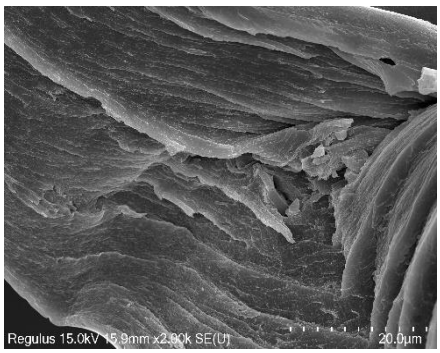

C - SEM image of a sample of GelMAX+LAP

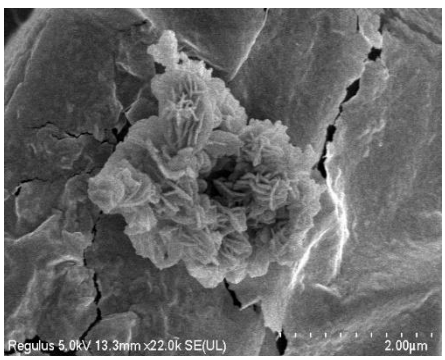

D - SEM image of a MXene in GelMA+MX+LAP

Figure 4.9 — SEM Images of each group's sample (A-C); C - MXenes are homogeneous in this group; D - MXenes are heterogenous in this group more likely to be in clusters

folded morphology. When the MXenes are more clearly homogeneous in the sample, their presence modifies the structure. Figure 4.9 C shows a more stratified and smoother morphology than the other two. The stratified morphology is due to the MXenes being integrated into the synthesis of the GelMA; they get to be much more homogeneous, giving that morphology to the sample. The MXenes have stratified morphology as a characteristic of themselves, like in Figure 4.9 C. Figure 4.9 D represented another way that the MXenes can present themselves, in this case, was seen when the MXenes were heterogenous and not integrated into the synthesis.

The SEM images presented in Figure 4.9 A and B demonstrate the existence of an isotropic structure, which is typified by randomly dispersed pores that lack a defined orientation within the hydrogel matrix. The materials in these samples appear favorable to uniform diffusion and cell infiltration in all directions based on the disordered porosity. On the other hand, Figure 4.9C shows an anisotropic structure with unidirectionally ordered pores. This directed configuration implies a more organized internal structure that could offer enhanced mechanical properties or specific guidance for cell movement and nutrient transport along the aligned pathways [105].

4.3.3 Atomic Force Microscopy (AFM)

The Young's modulus of three different types of hydrogels was measured using Atomic Force Microscopy (AFM), as shown in Figure 4.10.

The results indicate that Young's modulus of GelMA hydrogel is significantly higher when compared with the other hydrogels. GelMA+LAP is a stiff hydrogel with a wide range of modulus values, indicating that it may be too inflexible for certain cardiac applications. The cardiac tissue needs to strike a balance between elasticity for contraction and relaxation, and stiffness for structural support. If materials are overly rigid, they can hinder the movement of heart cells. While the stiffness may need to be adjusted for cardiac patches or scaffolds, it might be suitable for applications that prioritize mechanical strength [106-108].

GelMA+MX hydrogel, with Young's modulus of 10 kPa, is suitable for cardiac applications due to its resemblance to the heart's natural mechanical environment. This decreased stiffness facilitates better cell spreading, migration, and contraction, making it an ideal choice for cardiac tissue engineering due to its flexibility and intended stiffness range [106-108].

GelMAX has a moderate Young's modulus, ranging from 15 to 20 kPa. This number falls within the stiffness range of the heart tissue. The intermediate stiffness suggests a balance between rigidity and flexibility for heart tissue scaffolds. This hydrogel might enable the

required tissue movement while offering sufficient structural support. Because GelMAX provides an excellent balance between stiffness and flexibility, it is a promising material for cardiac tissue engineering. It may sustain mechanical and cellular functions such as contraction [106-108].

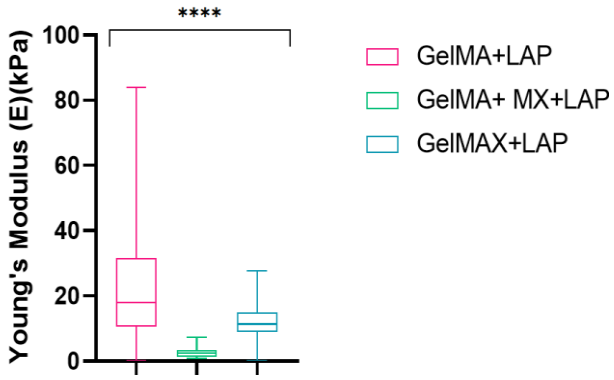

Figure 4.10 — Graphic of Young's modulus measured with Atomic Force Microscopy for hydrogels before being in cell culture, **** p<0.0001

MXene nanoparticles significantly improve the mechanical properties of hydrogels utilized in cardiac tissue engineering. Renowned for their exceptional electrical conductivity and mechanical strength, MXenes have been integrated into GelMA+MX and GelMAX hydrogels to enhance their performance, particularly in promoting electrical signaling among cardiomyocytes.

Although GelMA, which does not contain MXenes, exhibits the highest Young's modulus, its stiffness surpasses the natural range found in heart tissue, thereby limiting its suitability. In contrast, GelMA+MX presents a lower Young's modulus, aligning more closely with the stiffness of healthy cardiac tissue, which enhances both flexibility and mechanical support. The electrical conductivity of MXenes further facilitates the synchronized beating of cardiomyocytes, an essential factor in tissue regeneration.

GelMAX provides an intermediate stiffness, striking a balance between rigidity and flexibility, making it potentially appropriate for cardiac applications that require additional mechanical support. Overall, GelMA+MX and GelMAX are more flexible hydrogels that better mimic the soft nature of the heart and promote critical cellular behaviors such as migration and differentiation.

4.4 Cellular Assays

4.4.1 Cell Culture

Once the scaffold has been characterized, it is critical to evaluate its biocompatibility and how it interacts with cells. The tests aim to assess its suitability as structural support for tissue formation and cell adhesion.

In the first experiment involving cell culture, the groups studied were GelMA and GelMA+MX; GelMAX was not included due to its synthesis, which was not yet ready at the time. In a well plate of 12 wells, 8 were coated with 0.5ml of bioink+cells, 4 of each available sample, and then each well was crosslinked with the nails lamp (365 nm + 405 nm) for 60 s (Figure 4.6).

In the second experiment, cell culture was made in a 24-well plate to reduce the amount of material used, the swelling, and because the swelling tests were done with less amount of material. 15 wells with coverslips were coated with 200 µL of bioink+cells, and 5 of each group including the GelMAX group. The crosslinking time chosen for this cell culture was 2 minutes in each well since the swelling visual test this time and above was more stable (Figure 4.11).

Human fibroblasts were used as a cost-effective alternative to hiPSCs for the third time doing cell culture, given the high cost associated with hiPSC cell lines. Fibroblasts, in addition

Figure 4.11 — Second Cell Culture; The samples with white color are the group of GelMA+LAP+Cells; The other samples with black dots are the group of GelMA+MX+LAP+Cells; GelMAX+LAP+Cells are the black samples without dots. All of them were exposed for 2min.

to being more cost-effective, are also found in human heart tissue. The cell culture was made on a 12-well plate. 3 wells with coverslips were coated with 200 µL of the bioink available at the time (GelMAX) and $1x10^5$ cells. Then they were crosslinked with a UV lamp (365 nm) for 5 min, 9 min, and 12 min, to see if a UV lamp with only one wavelength and increasing the

crosslinking time would make a difference in the cell viability. After being crosslinked and before placing the medium in the well, the scaffolds were washed with PBS.

4.4.2 Live/Dead Staining

A viability/toxicity kit was used to assess the scaffolds' viability with cells. When the live cells were stained with calcein, they emitted a green fluorescence; when the DNA of the dead cells was bound to the ethidium-1 homodimer, it emitted a red fluorescence. It is essential to highlight that the cells were incorporated into the scaffolds to minimize the loss of cells that might otherwise adhere to the culture medium or the well instead of attaching to the scaffold if they were merely seeded. This has been a challenge that others in the department have encountered in the past.

In the first experiment involving cell culture, the unexpected swelling of the scaffolds (Figure 4.6) led to the "disappearance" of the cells. This swelling led to poor cell-bioink interaction. Supporting the fact that the cells could not attach themselves to the material and remained in the culture medium. By staying in the culture medium, they were aspirated when it was changed, so there was no fluorescence signal from calcein or ethidium homodimer-1 when the Live/Death test was carried out (Figure A.5).

Afterward, the bioinks were improved, and the swelling tests and a new culture with cardiomyocytes were carried out. When the images were obtained, no signal was visible. However, the signal was weak, and both green and red signals overlapped. This may be due to the thickness of the hydrogel, which may need more time for the proper fluorophores' penetration. In addition, the lack of signal detection by the microscope and the high hydrogels' thickness may caused issues in observing all planes to obtain a signal (Figure A.5).

One of the hypotheses as to why the cells were not detected may be that the groups in GelMA were not functionalized by the groups in the LAP photoinitiator; these non-crosslinked groups may promote cells' toxicity over the culture time, resulting in cell death. These non-functionalized groups may also have contributed to some cells not adhering and proliferating in the scaffold. Whenever the culture medium was changed, the cells that had not managed to adhere to and proliferate in the scaffold remained in the culture medium and consequently ended up disappearing, thus reducing the number of cells present at the end of the 7 days of cell culture. Leaving only those who managed to adhere and were not affected by the non-functionalized groups [114].

This leads us to believe that a longer exposure time to UV light would be necessary to reduce the likelihood of these groups becoming free because they are not functionalized, or

instead of increasing the exposure time after crosslinking, washing the scaffolds with PBS would remove some of the non-functionalized groups and thus reduce the chance of cell death, which would consequently help their adhesion and proliferation [114].

Nguyen et al. found that non-functionalized LAP groups produce reactive oxygen species (ROS), potentially causing membrane poration in bioprinting with photopolymers. The photosensitization screening method showed increased LAP concentrations increased photocatalytic potential, suggesting membrane poration. Increased ultraviolet exposure has diminished the photocatalytic potential. [114].

For the third time doing cell culture, this time in fibroblasts, and having the crosslinking time more optimized (5min, 9min, and 12min) helped to prevent the swelling as in the first experiment and minimize the ROS of the LAP. The live dead performed in the samples available show some Live/Dead signals but not a clear one (Figure A.6). This suggests that the protocol needs to be adjusted to these hydrogels, and the cell-bioink interaction needs to be improved to not be cytotoxic to the cells. Because the thickness of the hydrogels doesn't allow the microscope to penetrate all the planes to obtain a signal, samples could be cut to help have better images for live/dead. Therefore, equation 3 mentioned in section 3.8.2 cannot be used to determine cell viability.

4.4.3 Presto Blue Assay

This assay has the purpose of evaluating the metabolic activity in the 3 groups (GelMA, GelMA+MX, and GelMAX). Since the first cell culture showed no sign in life/death, the presto blue also showed no metabolic activity, for the same reason. The cells have died from the ROS created by the LAP photoinitiator. From the graph presented in Figure 4.12, we can conclude that the increased exposure to UV light led to an improvement in metabolic activity, compared to the first cell culture which showed no metabolic activity. However, this metabolic activity was reduced in the groups with cells compared to the positive control (Medium+Cells). The groups without cells (GelMA+Medium and GelMAX+Medium) showed slightly higher metabolic activity than the groups with cells (GelMA+Cells and GelMAX+Cells). This suggests a poor interaction between the cells and the bioink materials, leading to a reduction in metabolic performance. Concerning the GelMA+MX+Cells group, it shows metabolic activity because it is higher than the GelMA+MX+Medium group without cells, which leads us to believe that there was better interaction between the cells and the bioink materials, but even so there was some poor interaction between the cells and the bioink materials because otherwise the metabolic activity values of the GelMA+MX+Cells group would be closer to those of the positive

control (Medium+Cells). Figure 4.12 is a result of the active trying to resolve the problem confronted in the previous cell cultures, by increasing the time exposure, and the amount of cells per well and decreasing the volume of hydrogel used in each well. Although the results can be

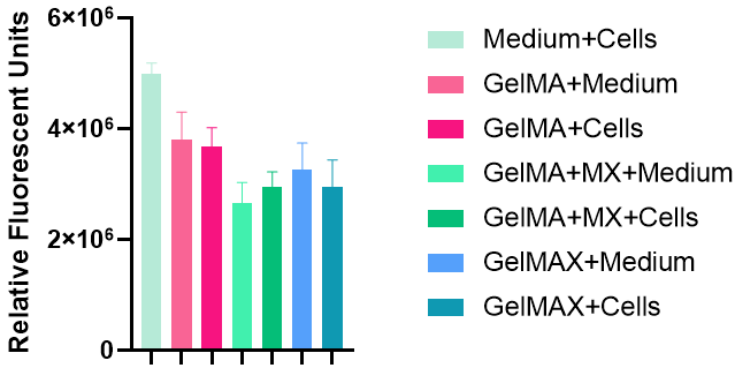

Figure 4.12 — Graphic of the relative fluorescent units for the 7th day of the second cell culture, resulting from the Presto Blue assay

considered successful, there is room for improvement. Increasing the exposure time could help reduce ROS production from LAP, and washing the hydrogels after crosslinking would likely enhance metabolic activity. Relatively to the third time the cell culture was made, presto blue was performed but didn't show any metabolic activity, suggesting that the protocol needs to be optimized.

4.4.4 Immunofluorescence

DAPI and Phalloidin are used in immunofluorescence staining to simultaneously visualize the nucleus (with DAPI) and the cytoskeleton (with Phalloidin). The first experiment involving cell culture immunofluorescence assay was performed, and there was no signal transmission from the fluorophores. The second experiment involving cell culture immunofluorescence analysis was also carried out, but only for 2 of the 3 groups once the GelMAX samples had broken up into very small pieces making it impossible to see the fluorophore signal in the confocal technique. Immunofluorescence was carried out on the remaining groups (GelMA and GelMA+MX) and as well as in the previous experiments with cell culture, none of the fluorophores transmitted a significant signal. This indicates poor penetration of the fluorophores into the samples. To avoid this limitation, in the third experiment involving cell culture, the fluorophores were left to act for longer to ensure their total penetration into the samples. Even though some signal was detected, only reasonable images were obtained from Phalloidin since unviable images were sourced from DAPI. Due to the specifications of the samples, there were different penetrations of DAPI in each plane, which made it challenging to observe with the

confocal microscope. Figure A.7 shows that the cells are present, and their cytoskeleton is marked with phalloidin. The cells seem to have managed to penetrate and sustain themselves on the scaffolds. The cells on the scaffold exposed to UV for 5 minutes appear to be more clustered than the cells present on the other scaffolds with more time of UV exposure, 9 minutes and 12 minutes. With the images present in Figure A.7, it can be concluded that the 9min and 12min of exposure times are promising to test/use on hiPSCs without cell death occurring. To be certain of the exact exposure time that the biotin no longer interacts negatively with the cells, more tests need to be carried out with a cell culture that is less expensive than the hiPSC culture, such as the human-derived fibroblast culture.

4.4.5 Scanning Electron Microscopy after Cell Culture

Considering that the tests carried out so far, such as Live/Dead, Presto Blue, and Immunofluorescence did not show any signs of cell viability, metabolic activity, DNA marking, or cytoskeleton. SEM was performed to ensure whether the scaffolds showed any cell morphology, which could be present or have been present in them, (Figure 4.13 and Figure 4.14). SEM was only carried out on the samples from the first cell culture, containing only the GelMA and GelMA+MX groups. The GelMAX group remained to be seen in the SEM. In the second experiment involving cell culture, it was not possible to make the group that remained because the GelMAX samples were too small to dry with ethanol and prevent them from being aspirated during the change of dilutions. Therefore, only the GelMA and GelMA+MX groups were analyzed by SEM. Cross-section images are presented in Figure 4.13 and Figure 4.14.

In Figure 4.13, there are changes to the surface compared to Figure 4.9A, where there are no cells. It is possible to see various clusters of cells and extracellular matrix, which leaves

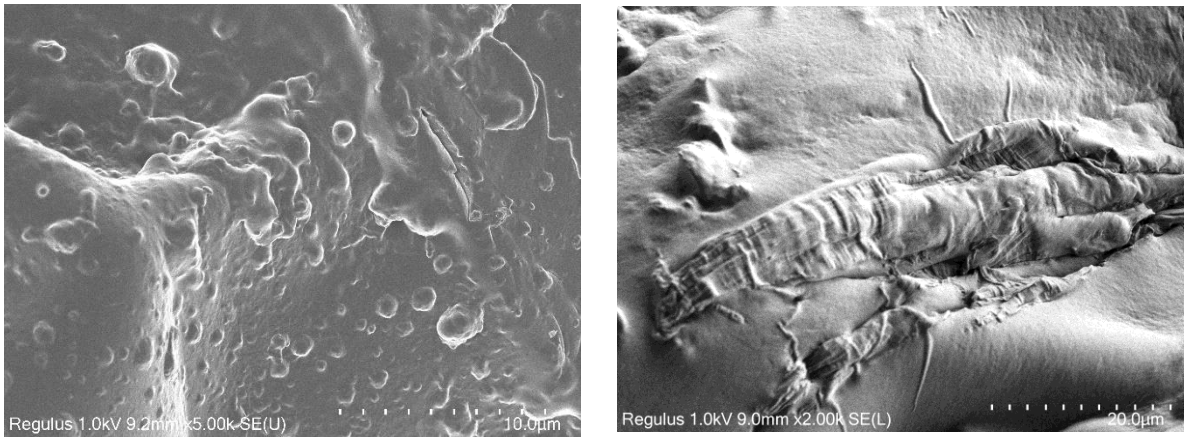

Figure 4.13 — SEM images of a transversal cut of GelMA+LAP+Cells

the surface with a different type of roughness as shown in Figure 4.9A. This may indicate that

the cells were either present during the SEM analysis or had detached due to swelling and weak cell-bioink Interaction. Another feature that can be seen in Figure 4.13 and Figure 4.14 is the fact that the cells are protected by the hydrogel as if they had a cover around them. This is because the cells are embedded in the hydrogel and not seeded as in recent studies. The image on the right side of Figure 4.13 shows a more elongated type of cell, suggesting it is a hiPSC-derived cardiomyocyte. This is because of its more elongated structure, and despite having a layer of hydrogel on top, some characteristic sarcomere bands of cardiomyocytes [109].

The left-hand image in Figure 4.14 also shows clusters and extracellular material, similar to Figure 4.13, but also highlights an intermediate phase between differentiated and undifferentiated cells. These cells exhibit an oval, flattened morphology (indicated by arrows), in contrast to the more spherical or elongated shapes seen previously. The right-hand image in Figure 4.14 shows both agglomerated and non-agglomerated human induced pluripotent stem cells. Additionally, the surface layer covering the cells displays a more sinuous texture compared to the images in Figure 4.13, possibly due to the presence of MXenes in the sample. Although no titanium was detected via EDS analysis, the MXenes are visibly present, as evidenced by the color change from white to a grey tone in the GelMA+MX samples and the visible clusters of MXene flakes.

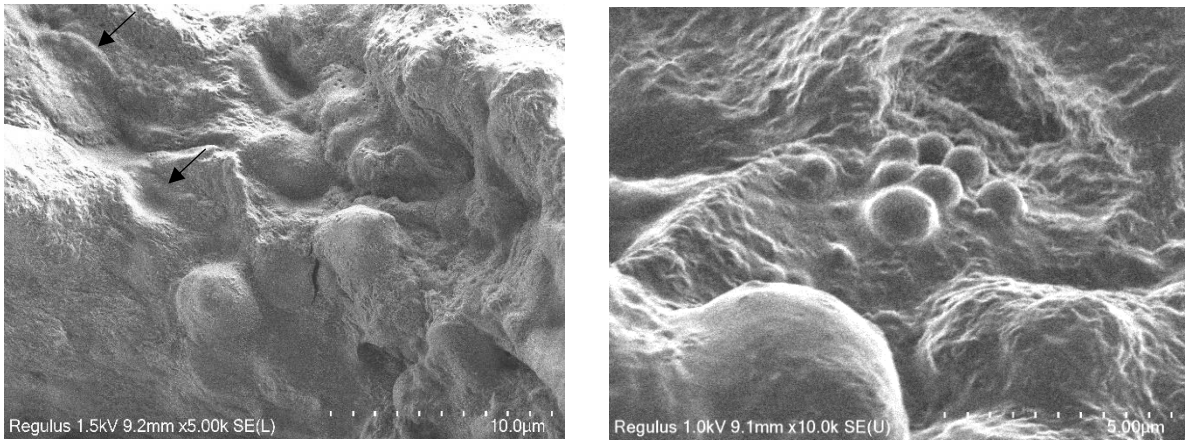

Figure 4.14 — SEM images of a transversal cut of GelMA+MX+LAP+Cells

4.4.6 AFM after Cell Culture

AFM was performed on the samples after cell culture to assess any changes in the mechanical properties. As visible in Figure 4.15 the stiffness of the hydrogels drastically reduced to ≤1 kPa, indicating a substantial decrease from the initial modulus shown in Figure 4.10 where the samples were subjected to the same mechanical test after being in the cell culture. GelMAX could not be evaluated after the cell culture because was too degraded, leaving Insufficient material for analysis.

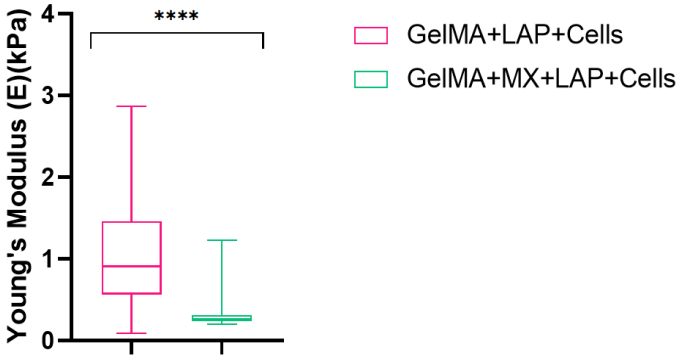

Figure 4.15 — Graphic of Young's modulus measured with Atomic Force Microscopy for hydrogels after being in cell culture, **** p<0.0001

The observed decrease in Young's modulus indicates that the presence of cells, along with potential degradation of the hydrogel over time, leads to a softening of the matrix. As previously discussed, incomplete activation of the photoinitiator (LAP) and methacrylate groups in GelMA—likely due to insufficient exposure time or inadequate lamp intensity—may have resulted in unreacted groups. This lack of complete reaction could contribute to cell toxicity, further accelerating the degradation of the hydrogel and resulting in its softening. The graph in Figure 4.15 illustrates how this softening reflects the dynamic interaction between the cells and the hydrogel matrix.

4.5 In vitro Model

Unfortunately, due to time constraints and poor cell-bioink interaction, the project was not ready to progress on to the next phase - the development of an in vitro arrhythmia model. While cell-material interactions had been successfully tested in 2D, the transition to 3D proved to be challenging. The insufficient interaction between the cells and the materials made it impossible to proceed with the arrhythmia model and its electrical stimulation. The use of 3D culture is critical, as it is more accurate it essential for creating a realistic cardiac model. Further improvements in the 3D environment are required to achieve this goal.

5

Conclusions and Future Work

By constructing a 3D support that resembles the extracellular matrix of the heart, the dissertation research hopes to accelerate the maturation of cardiomyocytes. Despite its theoretically low conductivity, GelMA, a biodegradable polymer, is utilized in tissue engineering applications. The choice of MXenes was driven by their biocompatibility and conductive properties, which demonstrate significant potential for cardiac tissue engineering (CTE). Given that the scaffold's structure closely resembles that of native heart tissue, biomaterials with adjustable properties are essential. The incorporation of MXenes enhances the stability and mechanical attributes of the structure. To ascertain non-toxicity and porosity, it is necessary to characterize the structures in terms of their physicochemical properties. A viability study is essential to verify the biocompatibility of the scaffold, assess its positive effects on cardiac cells, and ensure its effectiveness in tissue engineering.

Analysis of the hydrogels using Scanning Electron Microscopy (SEM) revealed aligned unidirectional pores, consistent with the anisotropic architecture of GelMAX, attributed to the incorporation of MXenes during GelMA synthesis. In contrast, the other samples, GelMA and GelMA+MX, exhibited an isotropic structure devoid of pore alignment. It was crucial to evaluate the electrical conductivity of these structures, given the conductive nature of the heart's extracellular matrix. Conductivity measurements indicated that GelMA and GelMA+MX had a higher conductivity (approximately 0.2 S/m) compared to GelMAX (0.1 S/m); however, GelMAX demonstrated conductivity levels that were closest to that of heart tissue (0.1 S/m). Further conductivity tests are necessary, particularly after the hydrogel has been cross-linked, to determine if there are significant changes in conductivity between the initial bioink and the final hydrogel.

It is well established that the contractility and rhythmic behavior of cardiomyocytes (CMs) diminish with increasing values of Young's modulus, which are regarded in the literature as overly rigid for cardiac tissue engineering. Among the tested materials, GelMA exhibited the highest Young's modulus, while GelMAX and GelMA+MX demonstrated lower values that fall within the optimal range for cardiac tissue applications. To characterize the nanoparticles (NPs)

used in these constructs, the solutions were analyzed using scanning electron microscopy (SEM). This analysis revealed that the integration of MXenes into the solutions interacts distinctly with GelMA, resulting in entirely different architectures. Additionally, the SEM findings suggest that achieving a homogeneous sample of MXenes is more straightforward in GelMAX, where the MXenes form an anisotropic architecture and are layered on top of one another. In contrast, with GelMA+MX, identifying the small clusters of MXenes presents a greater challenge.

Additionally, swelling—a characteristic associated with cell penetration—was evaluated. As anticipated and supported by the research findings, swelling decreases with increased exposure duration to the UV lamp. Alongside this, metabolic activity exhibited an upward trend with longer UV exposure times. Notably, the GelMA+MX+Cells group demonstrated that MXenes do not interfere with the cells' interaction with the substance; this group recorded higher metabolic activity values compared to the GelMA+MX+Medium group.

This dissertation indicates that the groups containing nanoparticles exhibit mechanical properties similar to those of the heart's extracellular matrix (ECM). Despite the need for further optimizations, nanoparticle bioinks show great promise for facilitating cardiomyocyte maturation.

Without optimizations pertaining to UV lamp exposure time, the cell viability protocol, and metabolic activity assessments, advancing to the arrhythmia model phase was not feasible due to the risks of cell death and insufficient maturation. Several setbacks contributed to this situation, including a two-month delay caused by initial bureaucratic processes and another two-month setback due to contamination in the cell laboratory. These delays limited the time available to thoroughly investigate and implement meaningful modifications to the cell-bioink interaction. Without a robust cell-bioink interaction, progressing to the subsequent step—the arrhythmia model and its electrical stimulation—was impractical.

To enhance this research, future efforts will need to focus on optimizing the placement of cells within the created scaffolds, alongside conducting tests on arrhythmic behavior induced by methyl- β -cyclodextrin (MBCD) and electrical stimulation to monitor the maturation of cardiac cells. Additionally, it will be crucial to establish a consensus on the optimal UV exposure time that balances safety with cardiomyocyte maturation, especially given the promising results observed with fibroblasts. Furthermore, it would be crucial to reduce the concentration of materials related to the formulation of bioinks to minimize waste, based on the concentrations suggested by S. Boularaoui et al. [103] for skeletal muscle tissues.

BIBLIOGRAPHY

[1] "Cardiovascular diseases." Accessed: Aug. 29, 2024. [Online]. Available: https://www.who.int/health-topics/cardiovascular-diseases#tab=tab_1

[2] K. Zhu *et al.*, "Human induced pluripotent stem cell (hipsc)-derived cardiomyocyte modelling of cardiovascular diseases for natural compound discovery," *Biomedicine & Pharmacotherapy*, vol. 157, p. 113970, Jan. 2023. doi:10.1016/j.biopha.2022.113970

[3] O. Mourad *et al.*, "Modeling heart diseases on a chip: Advantages and future opportunities," *Circulation Research*, vol. 132, no. 4, pp. 483–497, Feb. 2023. doi:10.1161/circresaha.122.321670

[4] A. I. van den Bulcke *et al.*, "Structural and Rheological Properties of Methacrylamide Modified Gelatin Hydrogels," *Biomacromolecules*, vol. 1, no. 1, pp. 31–38, 2000, doi: 10.1021/BM990017D.

[5] "American Heart Association | To be a relentless force for a world of longer, healthier lives." Accessed: Aug. 29, 2024. [Online]. Available: https://www.heart.org/

[6] "Arrhythmias - What Is an Arrhythmia? | NHLBI, NIH." Accessed: Aug. 29, 2024. [Online]. Available: https://www.nhlbi.nih.gov/health/arrhythmias

[7] J. Kingma *et al.*, "Overview of Cardiac Arrhythmias and Treatment Strategies," *Pharmaceuticals 2023, Vol. 16, Page 844*, vol. 16, no. 6, p. 844, Jun. 2023, doi: 10.3390/PH16060844.

[8] S. Colilla *et al.*, "Estimates of current and future incidence and prevalence of atrial fibrillation in the U.S. adult population," *The American journal of cardiology*, vol. 112, no. 8, pp. 1142–1147, Oct. 2013, doi: 10.1016/J.AMJCARD.2013.05.063.

[9] L. Staerk *et al.*, "Atrial Fibrillation: Epidemiology, Pathophysiology, and Clinical Outcomes," *Circulation research*, vol. 120, no. 9, pp. 1501–1517, Apr. 2017, doi: 10.1161/CIRCRESAHA.117.309732.

[10] H. Calkins *et al.*, "2017 HRS/EHRA/ECAS/APHRS/SOLAECE expert consensus statement on catheter and surgical ablation of atrial fibrillation," *Europace : European pacing, arrhythmias,*

and cardiac electrophysiology : journal of the working groups on cardiac pacing, arrhythmias, and cardiac cellular electrophysiology of the European Society of Cardiology, vol. 20, no. 1, pp. e1–e160, Jan. 2018, doi: 10.1093/EUROPACE/EUX274.

[11] J. Kingma *et al.*, "Overview of Cardiac Arrhythmias and Treatment Strategies," *Pharmaceuticals*, vol. 16, no. 6, Jun. 2023, doi: 10.3390/PH16060844.

[12] C. Mason and P. Dunnill, "A Brief Definition of Regenerative Medicine," *Regenerative Medicine*, vol. 3, no. 1, pp. 1–5, Jan. 2008, doi: 10.2217/17460751.3.1.1.

[13] "What Is Regenerative Medicine? – Regenerative Medicine at the McGowan Institute." Accessed: Aug. 29, 2024. [Online]. Available: https://mirm-pitt.net/about-us/what-is-regenerative-medicine/

[14] J. P. Fisher *et al.*, "Tissue Engineering," *Science*, pp. 1–583, Jan. 1993, doi: 10.1126/SCIENCE.8493529.

[15] F. J. O'Brien, "Biomaterials & scaffolds for tissue engineering," *Materials Today*, vol. 14, no. 3, pp. 88–95, Mar. 2011, doi: 10.1016/S1369-7021(11)70058-X.

[16] M. Sun *et al.*, "Synthesis and Properties of Gelatin Methacryloyl (GelMA) Hydrogels and Their Recent Applications in Load-Bearing Tissue," *Polymers 2018, Vol. 10, Page 1290*, vol. 10, no. 11, p. 1290, Nov. 2018, doi: 10.3390/POLYM10111290.

[17] G. Camci-Unal *et al.*, "Hydrogels for cardiac tissue engineering," *NPG Asia Materials 2014 6:5*, vol. 6, no. 5, pp. e99–e99, May 2014, doi: 10.1038/am.2014.19.

[18] E. Hoch *et al.*, "Stiff gelatin hydrogels can be photo-chemically synthesized from low viscous gelatin solutions using molecularly functionalized gelatin with a high degree of methacrylation," *Journal of Materials Science: Materials in Medicine*, vol. 23, no. 11, pp. 2607–2617, Nov. 2012, doi: 10.1007/S10856-012-4731-2.

[19] N. Annabi *et al.*, "Highly elastic micropatterned hydrogel for engineering functional cardiac tissue," *Advanced Functional Materials*, vol. 23, no. 39, pp. 4950–4959, Oct. 2013, doi: 10.1002/ADFM.201300570.

[20] M. Sun *et al.*, "Synthesis and Properties of Gelatin Methacryloyl (GelMA) Hydrogels and Their Recent Applications in Load-Bearing Tissue," *Polymers 2018, Vol. 10, Page 1290*, vol. 10, no. 11, p. 1290, Nov. 2018, doi: 10.3390/POLYM10111290.

[21] Z. Wang *et al.*, "Comparative study of gelatin methacrylate hydrogels from different sources for biofabrication applications," *Biofabrication*, vol. 9, no. 4, p. 044101, Aug. 2017, doi: 10.1088/1758-5090/AA83CF.

[22] J. W. Nichol *et al.*, "Cell-laden microengineered gelatin methacrylate hydrogels," *Biomaterials*, vol. 31, no. 21, pp. 5536–5544, Jul. 2010, doi: 10.1016/J.BIOMATERIALS.2010.03.064.

[23] K. Yue *et al.*, "Synthesis, properties, and biomedical applications of gelatin methacryloyl (GelMA) hydrogels," *Biomaterials*, vol. 73, pp. 254–271, Dec. 2015, doi: 10.1016/J.BIOMATERIALS.2015.08.045.

[24] F. Züger *et al.*, "Nanocomposites in 3D Bioprinting for Engineering Conductive and Stimuli-Responsive Constructs Mimicking Electrically Sensitive Tissue," *Advanced NanoBiomed Research*, vol. 2, no. 2, p. 2100108, Feb. 2022, doi: 10.1002/ANBR.202100108.

[25] M. L. Matias *et al.*, "3D printed MXene architectures for a plethora of smart applications," *Materials Today Advances*, vol. 23, p. 100512, Aug. 2024, doi: 10.1016/J.MTADV.2024.100512.

[26] G. Valurouthu *et al.*, "Tunable electrochromic behavior of titanium-based MXenes," *Nanoscale*, vol. 12, no. 26, pp. 14204–14212, Jul. 2020, doi: 10.1039/D0NR02673E.

[27] M. Lee *et al.*, "A Conductive and Adhesive Hydrogel Composed of MXene Nanoflakes as a Paintable Cardiac Patch for Infarcted Heart Repair," *ACS Nano*, vol. 17, no. 13, pp. 12290–12304, Jul. 2023, doi: 10.1021/ACSNANO.3C00933/SUPPL_FILE/NN3C00933_SI_008.MP4.

[28] H. Huang *et al.*, "Biomedical engineering of two-dimensional MXenes," *Advanced Drug Delivery Reviews*, vol. 184, p. 114178, May 2022, doi: 10.1016/J.ADDR.2022.114178.

[29] H. Lin *et al.*, "Insights into 2D MXenes for Versatile Biomedical Applications: Current Advances and Challenges Ahead," *Advanced Science*, vol. 5, no. 10, p. 1800518, Oct. 2018, doi: 10.1002/ADVS.201800518.

[30] H. Park *et al.*, "Bioactive inorganic compound MXene and its application in tissue engineering and regenerative medicine," *Journal of Industrial and Engineering Chemistry*, vol. 117, pp. 38–53, Jan. 2023, doi: 10.1016/J.JIEC.2022.10.014.

[31] G. Ye *et al.*, "Mussel-inspired conductive Ti_2C-cryogel promotes functional maturation of cardiomyocytes and enhances repair of myocardial infarction," *Theranostics*, vol. 10, no. 5, pp. 2047–2066, 2020, doi: 10.7150/THNO.38876.

[32] H. Zhu *et al.*, "Electroactive Oxidized Alginate/Gelatin/MXene (Ti3C2Tx) Composite Hydrogel with Improved Biocompatibility and Self-Healing Property," *Polymers*, vol. 14, no. 18, p. 3908, Sep. 2022, doi: 10.3390/POLYM14183908/S1.

[33] G. Basara *et al.*, "Electrically conductive 3D printed Ti3C2Tx MXene-PEG composite constructs for cardiac tissue engineering," *Acta Biomaterialia*, vol. 139, pp. 179–189, Feb. 2022, doi: 10.1016/J.ACTBIO.2020.12.033.

[34] B. D. Fairbanks *et al.*, "Photoinitiated polymerization of PEG-diacrylate with lithium phenyl-2,4,6-trimethylbenzoylphosphinate: polymerization rate and cytocompatibility," *Biomaterials*, vol. 30, no. 35, pp. 6702–6707, Dec. 2009, doi: 10.1016/J.BIOMATERIALS.2009.08.055.

[35] B. D. Fairbanks *et al.*, "A Versatile Synthetic Extracellular Matrix Mimic via Thiol-Norbornene Photopolymerization," *Advanced materials (Deerfield Beach, Fla.)*, vol. 21, no. 48, pp. 5005–5010, Dec. 2009, doi: 10.1002/ADMA.200901808.

[36] W. Schuurman *et al.*, "Gelatin-methacrylamide hydrogels as potential biomaterials for fabrication of tissue-engineered cartilage constructs," *Macromolecular bioscience*, vol. 13, no. 5, pp. 551–561, May 2013, doi: 10.1002/MABI.201200471.

[37] H. Xu*et al.*, "Effects of Irgacure 2959 and lithium phenyl-2,4,6-trimethylbenzoylphosphinate on cell viability, physical properties, and microstructure in 3D bioprinting of vascular-like constructs," *Biomedical Materials*, vol. 15, no. 5, p. 055021, Jul. 2020, doi: 10.1088/1748-605X/AB954E.

[38] A. García-Lizarribar *et al.*, "Composite biomaterials as long-lasting scaffolds for 3D bioprinting of highly aligned muscle tissue".

[39] S. Das *et al.*, "Gelatin Methacryloyl (GelMA)-Based Biomaterial Inks: Process Science for 3D/4D Printing and Current Status," *Biomacromolecules*, vol. 25, no. 4, pp. 2156–2221, Apr. 2024, doi: 10.1021/ACS.BIOMAC.3C01271/ASSET/IMAGES/MEDIUM/BM3C01271_0019.GIF.

[40] K. Zhu *et al.*, "Human induced pluripotent stem cell (hiPSC)-derived cardiomyocyte modelling of cardiovascular diseases for natural compound discovery," *Biomedicine & Pharmacotherapy*, vol. 157, p. 113970, Jan. 2023, doi: 10.1016/J.BIOPHA.2022.113970.

[41] M. Patterson *et al.*, "Frequency of mononuclear diploid cardiomyocytes underlies natural variation in heart regeneration," *Nature genetics*, vol. 49, no. 9, pp. 1346–1353, Sep. 2017, doi: 10.1038/NG.3929.

[42] T. Kitsuka *et al.*, "Advances in Cardiac Tissue Engineering," *Bioengineering 2022, Vol. 9, Page 696*, vol. 9, no. 11, p. 696, Nov. 2022, doi: 10.3390/BIOENGINEERING9110696.

[43] O. Bergmann *et al.*, "Evidence for cardiomyocyte renewal in humans," *Science (New York, N.Y.)*, vol. 324, no. 5923, pp. 98–102, Apr. 2009, doi: 10.1126/SCIENCE.1164680.

[44] M. A. Laflamme and C. E. Murry, "Heart regeneration," *Nature*, vol. 473, no. 7347, pp. 326–335, May 2011, doi: 10.1038/NATURE10147.

[45] H. v. Almeida *et al.*, "Human Extracellular-Matrix Functionalization of 3D hiPSC-Based Cardiac Tissues Improves Cardiomyocyte Maturation," *ACS Applied Bio Materials*, vol. 4, no. 2, pp. 1888–1899, Feb. 2021, doi: 10.1021/ACSABM.0C01490/ASSET/IMAGES/LARGE/MT0C01490_0004.JPEG.

[46] P. C. Baer *et al.*, "Fabrication and Characterization Techniques of In Vitro 3D Tissue Models," *International Journal of Molecular Sciences 2023, Vol. 24, Page 1912*, vol. 24, no. 3, p. 1912, Jan. 2023, doi: 10.3390/IJMS24031912.

[47] Y. Piao *et al.*, "Biomedical applications of gelatin methacryloyl hydrogels," *Engineered Regeneration*, vol. 2, pp. 47–56, Jan. 2021, doi: 10.1016/J.ENGREG.2021.03.002.

[48] L. Moroni *et al.*, "Biofabrication strategies for 3D in vitro models and regenerative medicine," *Nature Reviews Materials 2018 3:5*, vol. 3, no. 5, pp. 21–37, Apr. 2018, doi: 10.1038/s41578-018-0006-y.

[49] P. C. Baer *et al.*, "Fabrication and Characterization Techniques of In Vitro 3D Tissue Models," *International Journal of Molecular Sciences 2023, Vol. 24, Page 1912*, vol. 24, no. 3, p. 1912, Jan. 2023, doi: 10.3390/IJMS24031912.

[50] T. Xu *et al.*, "Complex heterogeneous tissue constructs containing multiple cell types prepared by inkjet printing technology," *Biomaterials*, vol. 34, no. 1, pp. 130–139, Jan. 2013, doi: 10.1016/J.BIOMATERIALS.2012.09.035.

[51] S. v. Murphy and A. Atala, "3D bioprinting of tissues and organs," *Nature biotechnology*, vol. 32, no. 8, pp. 773–785, 2014, doi: 10.1038/NBT.2958.

[52] Y. S. Zhang *et al.*, "Bioprinting 3D microfibrous scaffolds for engineering endothelialized myocardium and heart-on-a-chip," *Biomaterials*, vol. 110, pp. 45–59, Dec. 2016, doi: 10.1016/J.BIOMATERIALS.2016.09.003.

[53] C. Mandrycky *et al.*, "3D bioprinting for engineering complex tissues," *Biotechnology advances*, vol. 34, no. 4, pp. 422–434, Jul. 2016, doi: 10.1016/J.BIOTECHADV.2015.12.011.

[54] F. Pampaloni *et al.*, "The third dimension bridges the gap between cell culture and live tissue," *Nature reviews. Molecular cell biology*, vol. 8, no. 10, pp. 839–845, Oct. 2007, doi: 10.1038/NRM2236.

[55] A. D. Cigan *et al.*, "High seeding density of human chondrocytes in agarose produces tissue-engineered cartilage approaching native mechanical and biochemical properties," *Journal of biomechanics*, vol. 49, no. 9, p. 1909, Jun. 2016, doi: 10.1016/J.JBIOMECH.2016.04.039.

[56] U. A. Gurkan *et al.*, "Engineering anisotropic biomimetic fibrocartilage microenvironment by bioprinting mesenchymal stem cells in nanoliter gel droplets," *Molecular Pharmaceutics*, vol. 11, no. 7, pp. 2151–2159, Jul. 2014, doi: 10.1021/MP400573G/SUPPL_FILE/MP400573G_SI_010.PDF.

[57] R. Suntornnond *et al.*, "Bioprinting of Thermoresponsive Hydrogels for Next Generation Tissue Engineering: A Review," *Macromolecular Materials and Engineering*, vol. 302, no. 1, p. 1600266, Jan. 2017, doi: 10.1002/MAME.201600266.

[58] M. Mobaraki *et al.*, "Bioinks and bioprinting: A focused review," *Bioprinting*, vol. 18, p. e00080, Jun. 2020, doi: 10.1016/J.BPRINT.2020.E00080.

[59] J. D. Kim *et al.*, "Piezoelectric inkjet printing of polymers: Stem cell patterning on polymer substrates," *Polymer*, vol. 51, no. 10, pp. 2147–2154, May 2010, doi: 10.1016/J.POLYMER.2010.03.038.

[60] N. A. Sears *et al.*, "A Review of Three-Dimensional Printing in Tissue Engineering," *https://home.liebertpub.com/teb*, vol. 22, no. 4, pp. 298–310, Apr. 2016, doi: 10.1089/TEN.TEB.2015.0464.

[61] O. A. Mohamed *et al.*, "Optimization of fused deposition modeling process parameters: a review of current research and future prospects," *Advances in Manufacturing*, vol. 3, no. 1, pp. 42–53, Mar. 2015, doi: 10.1007/S40436-014-0097-7/METRICS.

[62] R. F. Pereira and P. J. Bártolo, "3D bioprinting of photocrosslinkable hydrogel constructs," *Journal of Applied Polymer Science*, vol. 132, no. 48, Dec. 2015, doi: 10.1002/APP.42458.

[63] T. Jungst *et al.*, "Strategies and Molecular Design Criteria for 3D Printable Hydrogels," *Chemical Reviews*, vol. 116, no. 3, pp. 1496–1539, Feb. 2016, doi: 10.1021/ACS.CHEMREV.5B00303/ASSET/ACS.CHEMREV.5B00303.FP.PNG_V03.

[64] T. Xu *et al.*, "Viability and electrophysiology of neural cell structures generated by the inkjet printing method," *Biomaterials*, vol. 27, no. 19, pp. 3580–3588, Jul. 2006, doi: 10.1016/J.BIOMATERIALS.2006.01.048.

[65] E. Hoch *et al.*, "Chemical tailoring of gelatin to adjust its chemical and physical properties for functional bioprinting," *Journal of Materials Chemistry B*, vol. 1, no. 41, pp. 5675–5685, Oct. 2013, doi: 10.1039/C3TB20745E.

[66] S. Knowlton *et al.*, , "Bioprinting for cancer research," *Trends in Biotechnology*, vol. 33, no. 9, pp. 504–513, Sep. 2015, doi: 10.1016/J.TIBTECH.2015.06.007/ASSET/AD96F2EE-E3AB-43E5-9B69-6A69285770FE/MAIN.ASSETS/GR5.SML.

[67] R. E. Saunders and B. Derby, "Inkjet printing biomaterials for tissue engineering: bioprinting," *International Materials Reviews*, vol. 59, no. 8, pp. 430–448, Nov. 2014, doi: 10.1179/1743280414Y.0000000040.

[68] V. Mironov *et al.*, "Organ printing: Computer-aided jet-based 3D tissue engineering," *Trends in Biotechnology*, vol. 21, no. 4, pp. 157–161, Apr. 2003, doi: 10.1016/S0167-7799(03)00033-7.

[69] J. Zhang *et al.*, "Three-dimensional printing of strontium-containing mesoporous bioactive glass scaffolds for bone regeneration," *Acta Biomaterialia*, vol. 10, no. 5, pp. 2269–2281, May 2014, doi: 10.1016/J.ACTBIO.2014.01.001.

[70] N. Jones, "Science in three dimensions: the print revolution," *Nature*, vol. 487, no. 7405, pp. 22–23, 2012, doi: 10.1038/487022A.

[71] Y. Wang *et al.*, "Effects of Hydroxyapatite and Hypoxia on Chondrogenesis and Hypertrophy in 3D Bioprinted ADMSC Laden Constructs," *ACS Biomaterials Science and Engineering*, vol. 3, no. 5, pp. 826–835, May 2017, doi: 10.1021/ACSBIOMATERIALS.7B00101.

[72] M. G. Yeo and G. H. Kim, "A cell-printing approach for obtaining hASC-laden scaffolds by using a collagen/polyphenol bioink," *Biofabrication*, vol. 9, no. 2, Apr. 2017, doi: 10.1088/1758-5090/AA6997.

[73] R. Xiong *et al.*, "Study of gelatin as an effective energy absorbing layer for laser bioprinting," *Biofabrication*, vol. 9, no. 2, Jun. 2017, doi: 10.1088/1758-5090/AA74F2.

[74] N. E. Fedorovich *et al.*, "Three-dimensional fiber deposition of cell-laden, viable, patterned constructs for bone tissue printing," *Tissue engineering. Part A*, vol. 14, no. 1, pp. 127–133, Jan. 2008, doi: 10.1089/TEN.A.2007.0158.

[75] N. E. Fedorovich *et al.*, "The Role of Endothelial Progenitor Cells in Prevascularized Bone Tissue Engineering: Development of Heterogeneous Constructs," *https://home.liebertpub.com/tea*, vol. 16, no. 7, pp. 2355–2367, Apr. 2010, doi: 10.1089/TEN.TEA.2009.0603.

[76] N. E. Fedorovich *et al.*, "Scaffold Porosity and Oxygenation of Printed Hydrogel Constructs Affect Functionality of Embedded Osteogenic Progenitors," *https://home.liebertpub.com/tea*, vol. 17, no. 19–20, pp. 2473–2486, Jul. 2011, doi: 10.1089/TEN.TEA.2011.0001.

[77] N. E. Fedorovich *et al.*, "Biofabrication of osteochondral tissue equivalents by printing topologically defined, cell-laden hydrogel scaffolds," *Tissue engineering. Part C, Methods*, vol. 18, no. 1, pp. 33–44, Jan. 2012, doi: 10.1089/TEN.TEC.2011.0060.

[78] F. Maiullari *et al.*, "A multi-cellular 3D bioprinting approach for vascularized heart tissue engineering based on HUVECs and iPSC-derived cardiomyocytes," *Scientific reports*, vol. 8, no. 1, Dec. 2018, doi: 10.1038/S41598-018-31848-X.

[79] D. J. Shiwarski *et al.*, "Emergence of FRESH 3D printing as a platform for advanced tissue biofabrication," *APL Bioengineering*, vol. 5, no. 1, p. 10904, Mar. 2021, doi: 10.1063/5.0032777.

[80] A. Lee *et al.*, "3D bioprinting of collagen to rebuild components of the human heart," *Science*, vol. 365, no. 6452, pp. 482–487, Aug. 2019, doi: 10.1126/SCIENCE.AAV9051/SUPPL_FILE/AAV9051S9.MP4.

[81] S. Catros *et al.*, "Laser-assisted bioprinting for creating on-demand patterns of human osteoprogenitor cells and nano-hydroxyapatite," *Biofabrication*, vol. 3, no. 2, Jun. 2011, doi: 10.1088/1758-5082/3/2/025001.

[82] H. Budharaju *et al.*, "Recent advancements in cardiovascular bioprinting and bioprinted cardiac constructs," *Biomaterials Science*, vol. 9, no. 6, pp. 1974–1994, Mar. 2021, doi: 10.1039/D0BM01428A.

[83] L. Ning *et al.*, "Characterization of Cell Damage and Proliferative Ability during and after Bioprinting," *ACS Biomaterials Science and Engineering*, vol. 4, no. 11, pp. 3906–3918, Nov. 2018, doi: 10.1021/ACSBIOMATERIALS.8B00714/SUPPL_FILE/AB8B00714_SI_001.PDF.

[84] A. I. van den Bulcke *et al.*, "Structural and rheological properties of methacrylamide modified gelatin hydrogels," *Biomacromolecules*, vol. 1, no. 1, pp. 31–38, 2000, doi: 10.1021/BM990017D.

[85] X. Wang *et al.*, "Correction: 3D Bioprinting Technologies for Hard Tissue and Organ Engineering. Materials 2016, 9, 802," *Materials 2016, Vol. 9, Page 911*, vol. 9, no. 11, p. 911, Nov. 2016, doi: 10.3390/MA9110911.

[86] I. T. Ozbolat and M. Hospodiuk, "Current advances and future perspectives in extrusion-based bioprinting," *Biomaterials*, vol. 76, pp. 321–343, 2016, doi: 10.1016/J.BIOMATERIALS.2015.10.076.

[87] D. Choudhury *et al.*, "The arrival of commercial bioprinters - Towards 3D bioprinting revolution!," *International journal of bioprinting*, vol. 4, no. 2, 2018, doi: 10.18063/IJB.V4I2.139.

[88] G. Kimbell and M. A. Azad, "3D printing: Bioinspired materials for drug delivery," *Bioinspired and Biomimetic Materials for Drug Delivery*, pp. 295–318, Jan. 2021, doi: 10.1016/B978-0-12-821352-0.00011-3.

[89] M. A. Azad *et al.*, "Polymers for Extrusion-Based 3D Printing of Pharmaceuticals: A Holistic Materials-Process Perspective," *Pharmaceutics*, vol. 12, no. 2, Feb. 2020, doi: 10.3390/PHARMACEUTICS12020124.

[90] H. Ramli *et al.*, "Basic principle and good practices of rheology for polymers for teachers and beginners," *Chemistry Teacher International*, vol. 4, no. 4, pp. 307–326, Dec. 2022, doi: 10.1515/CTI-2022-0010/DOWNLOADASSET/SUPPL/J_CTI-2022-0010_SUPPL.ZIP.

[91] A. GhavamiNejad *et al.*, "Crosslinking Strategies for 3D Bioprinting of Polymeric Hydrogels," *Small (Weinheim an der Bergstrasse, Germany)*, vol. 16, no. 35, Sep. 2020, doi: 10.1002/SMLL.202002931.

[92] S. v. Murphy *et al.*, "Evaluation of hydrogels for bio-printing applications," *Journal of Biomedical Materials Research Part A*, vol. 101A, no. 1, pp. 272–284, Jan. 2013, doi: 10.1002/JBM.A.34326.

[93] V. H. M. Mouser *et al.*, "Yield stress determines bioprintability of hydrogels based on gelatin-methacryloyl and gellan gum for cartilage bioprinting," *Biofabrication*, vol. 8, no. 3, Jul. 2016, doi: 10.1088/1758-5090/8/3/035003.

[94] D. Bonn *et al.*, "Yield stress materials in soft condensed matter," *Reviews of Modern Physics*, vol. 89, no. 3, p. 035005, Aug. 2017, doi: 10.1103/REVMODPHYS.89.035005/FIGURES/27/MEDIUM.

[95] P. A. Amorim *et al.*, "Insights on shear rheology of inks for extrusion-based 3D bioprinting," *Bioprinting*, vol. 22, p. e00129, Jun. 2021, doi: 10.1016/J.BPRINT.2021.E00129.

[96] J. Mewis and N. J. Wagner, "Thixotropy," *Advances in Colloid and Interface Science*, vol. 147–148, no. C, pp. 214–227, Mar. 2009, doi: 10.1016/J.CIS.2008.09.005.

[97] J. M. Townsend *et al.*, "Flow Behavior Prior to Crosslinking: The Need for Precursor Rheology for Placement of Hydrogels in Medical Applications and for 3D Bioprinting," *Progress in polymer science*, vol. 91, pp. 126–140, Apr. 2019, doi: 10.1016/J.PROGPOLYMSCI.2019.01.003.

[98] Z. Li *et al.*, "Proposal to assess printability of bioinks for extrusion-based bioprinting and evaluation of rheological properties governing bioprintability," *Biofabrication*, vol. 9, no. 4, p. 044107, Nov. 2017, doi: 10.1088/1758-5090/AA8DD8.

[99] J. M. Zuidema *et al.*, "A protocol for rheological characterization of hydrogels for tissue engineering strategies," *Journal of biomedical materials research. Part B, Applied biomaterials*, vol. 102, no. 5, pp. 1063–1073, 2014, doi: 10.1002/JBM.B.33088.

[100] A. Schwab *et al.*, "Printability and Shape Fidelity of Bioinks in 3D Bioprinting," *Chemical Reviews*, vol. 120, no. 19, pp. 11028–11055, Oct. 2020, doi: 10.1021/ACS.CHEMREV.0C00084/ASSET/IMAGES/LARGE/CR0C00084_0009.JPEG.

[101] Y. S. Zhang *et al.*, "3D Bioprinting for Tissue and Organ Fabrication," *Annals of biomedical engineering*, vol. 45, no. 1, pp. 148–163, Jan. 2017, doi: 10.1007/S10439-016-1612-8.

[102] S. M. Saraiva *et al.*, "Synthesis and characterization of a photocrosslinkable chitosan-gelatin hydrogel aimed for tissue regeneration," *RSC Advances*, vol. 5, no. 78, pp. 63478–63488, 2015, doi: 10.1039/C5RA10638A.

[103] S. Boularaoui *et al.*, "Nanocomposite Conductive Bioinks Based on Low-Concentration GelMA and MXene Nanosheets/Gold Nanoparticles Providing Enhanced Printability of Functional Skeletal Muscle Tissues," *ACS Biomaterials Science and Engineering*, vol. 7, no. 12, pp. 5810–5822, Dec. 2021, doi: 10.1021/ACSBIOMATERIALS.1C01193/ASSET/IMAGES/LARGE/AB1C01193_0009.JPEG.

[104] M. Y. Shie, J. J. Lee, C. C. Ho, S. Y. Yen, H. Y. Ng, and Y. W. Chen, "Effects of Gelatin Methacrylate Bio-ink Concentration on Mechano-Physical Properties and Human Dermal Fibroblast Behavior," *Polymers 2020, Vol. 12, Page 1930*, vol. 12, no. 9, p. 1930, Aug. 2020, doi: 10.3390/POLYM12091930.

[105] N. A. Jaya *et al.*, "Effect of anisotropic pores on the material properties of metakaolin geopolymer composites incorporated with corrugated fiberboard and rubber," *Journal of*

Materials Research and Technology, vol. 14, pp. 822–834, Sep. 2021, doi: 10.1016/J.JMRT.2021.06.098.

[106] P. Montero *et al.*, "Cells, Materials, and Fabrication Processes for Cardiac Tissue Engineering," *Frontiers in Bioengineering and Biotechnology*, vol. 8, p. 550810, Aug. 2020, doi: 10.3389/FBIOE.2020.00955/BIBTEX.

[107] M. Boffito, S. Sartori, and G. Ciardelli, "Polymeric scaffolds for cardiac tissue engineering: requirements and fabrication technologies," *Polymer International*, vol. 63, no. 1, pp. 2–11, Jan. 2014, doi: 10.1002/PI.4608.

[108] L. D. Huyer *et al.*, "Biomaterial based cardiac tissue engineering and its applications," *Biomedical Materials*, vol. 10, no. 3, p. 034004, May 2015, doi: 10.1088/1748-6041/10/3/034004.

[109] Y. Kanzaki *et al.*, "Images in Cardiovascular Medicine Three-Dimensional Architecture of Cardiomyocytes and Connective Tissue in Human Heart Revealed by Scanning Electron Microscopy," 2010, doi: 10.1161/CIRCULATIONAHA.110.979815.

[110] A. Polo-Montalvo *et al.*, "Effects of graphene oxide and reduced graphene oxide nanomaterials on porcine endothelial progenitor cells," *Nanoscale*, vol. 15, no. 42, pp. 17173–17183, Nov. 2023, doi: 10.1039/D3NR03145D.

[111] "Electrical conductivity of tissue at frequencies below 1 MHz Related content," 2009, doi: 10.1088/0031-9155/54/16/002.

[112] L. D. Huyer *et al.*, "Biomaterial based cardiac tissue engineering and its applications," *Biomedical Materials*, vol. 10, no. 3, p. 034004, May 2015, doi: 10.1088/1748-6041/10/3/034004.

[113] G. Gillispie *et al.*, "Assessment methodologies for extrusion-based bioink printability," *Biofabrication*, vol. 12, no. 2, p. 022003, Feb. 2020, doi: 10.1088/1758-5090/AB6F0D.

[114] A. K. Nguyen *et al.*, "Toxicity and photosensitizing assessment of gelatin methacryloyl-based hydrogels photoinitiated with lithium phenyl-2,4,6-trimethylbenzoylphosphinate in human primary renal proximal tubule epithelial cells," *Biointerphases*, vol. 14, no. 2, Mar. 2019, doi: 10.1116/1.5095886.

[115] G. A. Asaro *et al.*, "MXene functionalized collagen biomaterials for cardiac tissue engineering driving iPSC-derived cardiomyocyte maturation," *npj 2D Materials and Applications 2023 7:1*, vol. 7, no. 1, pp. 1–13, Jun. 2023, doi: 10.1038/s41699-023-00409-w.

[116] S. Bupphathong *et al.*, "Gelatin Methacrylate Hydrogel for Tissue Engineering Applications—A Review on Material Modifications," *Pharmaceuticals 2022, Vol. 15, Page 171*, vol. 15, no. 2, p. 171, Jan. 2022, doi: 10.3390/PH15020171.

[117] X. P. Li *et al.*, "Electrical stimulation of neonatal rat cardiomyocytes using conductive polydopamine-reduced graphene oxide-hybrid hydrogels for constructing cardiac microtissues," *Colloids and Surfaces B: Biointerfaces*, vol. 205, p. 111844, Sep. 2021, doi: 10.1016/J.COLSURFB.2021.111844.

A

ANNEX

A.1 3D Printing

The printed design is modeled at the software of CELLINK BIOX6 and is presented in Figure 3.4. The design is 4x4 cm in terms of length and width. Each square has 1x1 cm.

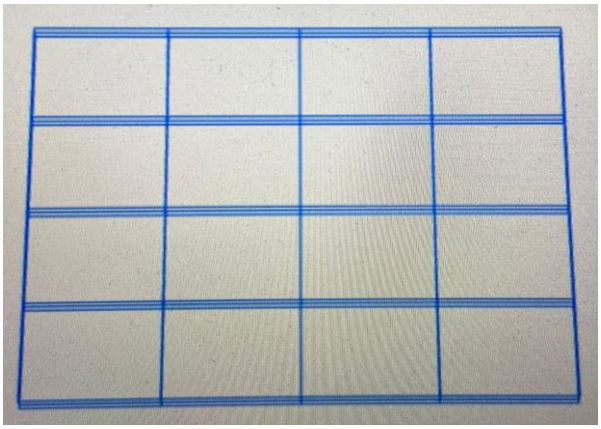

Figure A.1 — Design used for printability and printing accuracy tests.

A.2 AFM - sample placement

Placement of the sample for the AFM measurements.

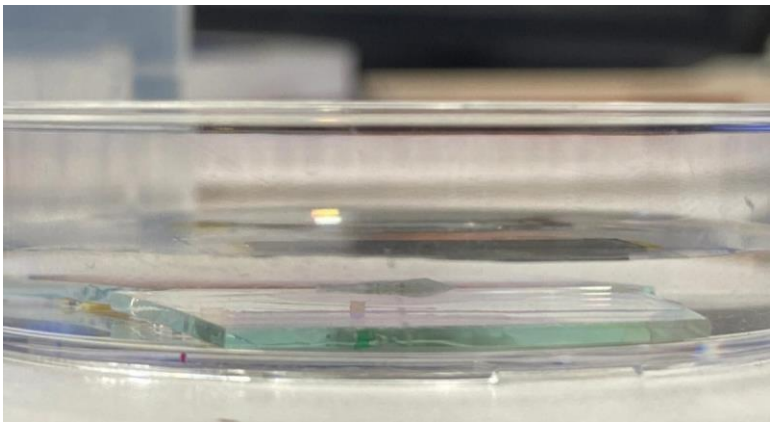

Figure A.2 — Hydrogel placement for AFM measurements

A.3 NMR Spectrum

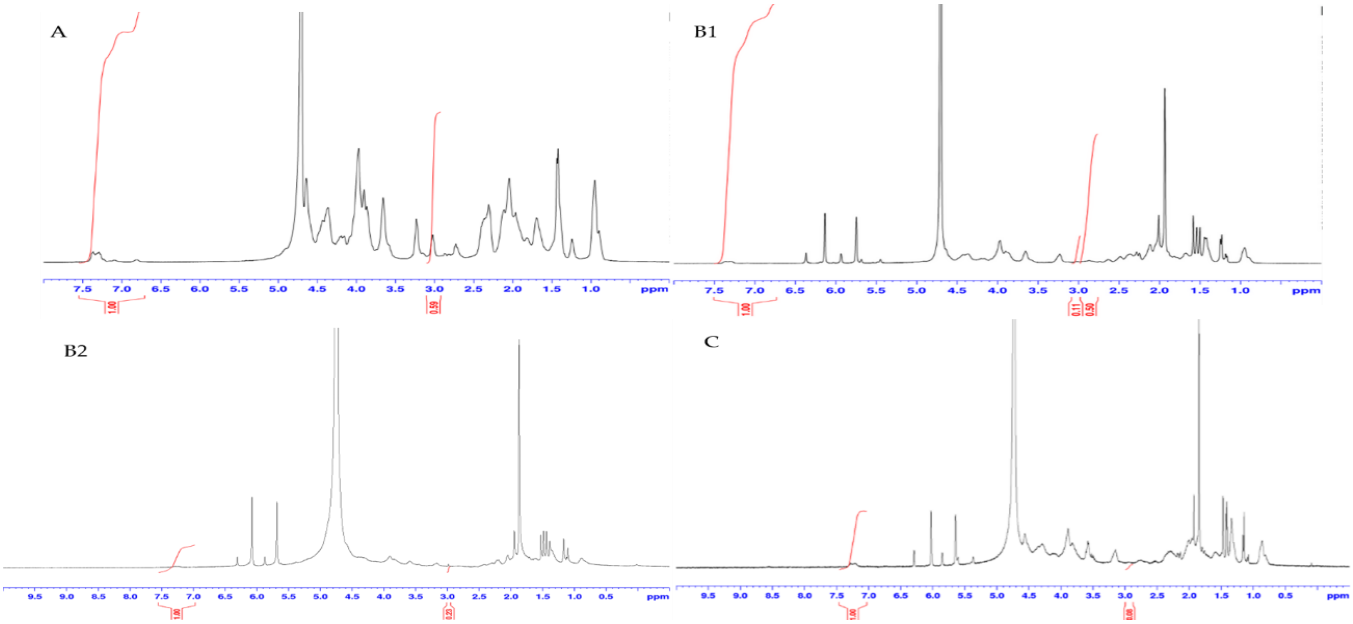

Figure A.3 — NMR Spectrums. A-NMR Spectrum of porcine Gelatin, gelatin unmodified; B1&B2 – NMR Spectrum of GelMA, gelatin modified; C – NMR Spectrum of GelMAX, gelatin modified with the nanoparticles Integrated In the synthesis

A.4 Swelling

Other times of UV exposure were tested for 2, 3, and 4 minutes with the UV lamp.

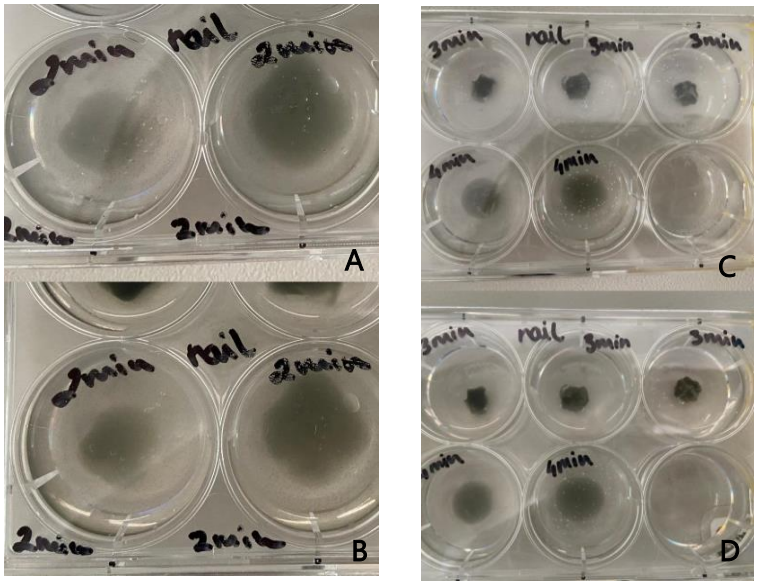

Figure A.4 — Visual swelling tests in some of the hydrogel groups. A and C 1st day at 37ºC; B and D 2nd day at 37ºC.

A.5 Live/Dead Signal

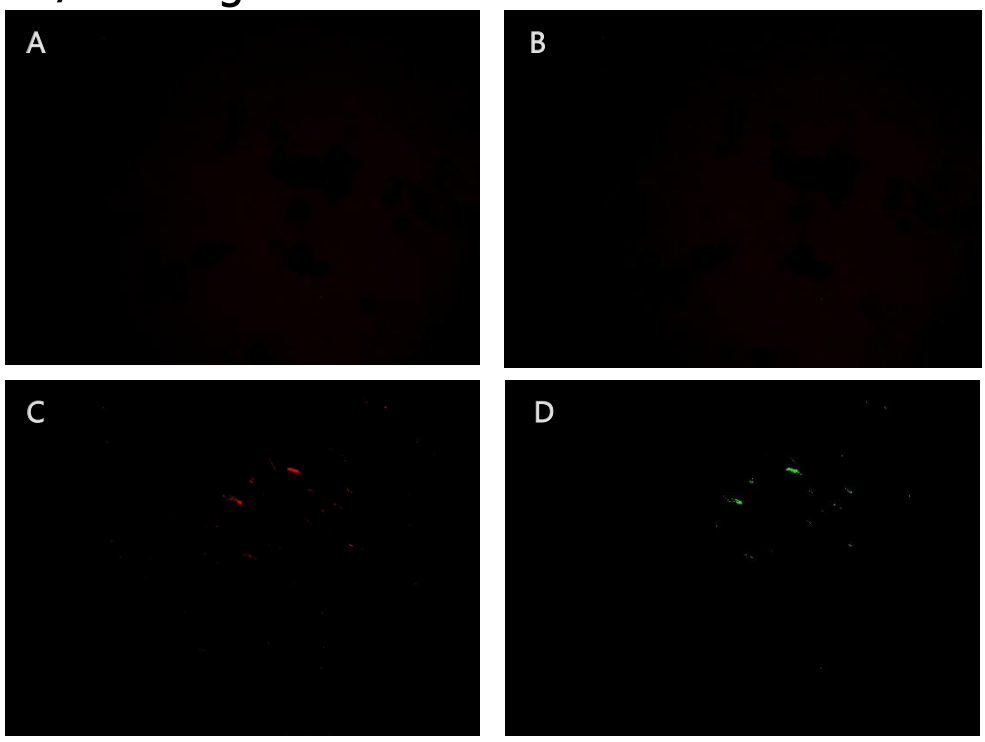

Figure A.5 — Some of the images taken of the Live/Dead Signal of the **first experiment involving cell culture** (A and B); A - Red signal of GelMA+MX; B - Green signal of GelMA+MX; Figures A and B show that there is no sign of any kind, either live or dead;

Live/Dead Signal of the **second experiment involving cell culture** (C and D); C - Red signal of GelMA; D - Green signal of GelMA; In Figures, C and D are visible that the Dead and Live signal are both in the same spots;

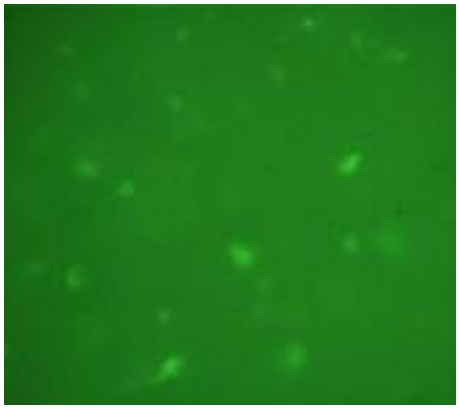

Figure A.6.1 — Image taken of the Live/Dead Signal of the **third experiment involving cell culture** (fibroblasts); Is visible some of live signal (green)

A.6 Phalloidin In Human Derived Fibroblasts

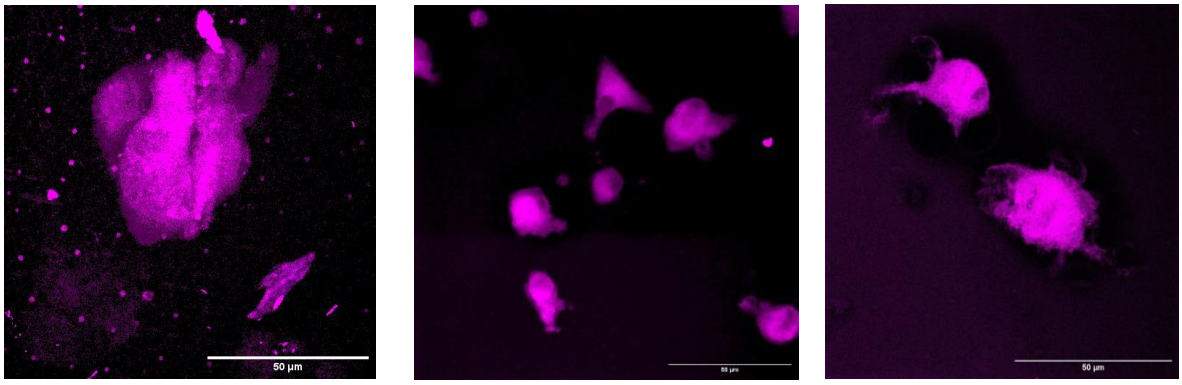

Figure A.7 — Images of Human Derived Fibroblasts containing Phalloidin. The image on the left had a 5 min of crosslinking time; the image in the middle had 9 min of crosslinking time; and the image on the right had 12 min of crosslinking time.